Measurement of the Casimir-Polder Force at Sub-micron Distance Scales using an Atomic Beam

A thesis
submitted for the Degree of
Doctor of Philosophy

in
The Faculty of Science
Bangalore University

by

D. Suresh

Indian Institute of Astrophysics
Bangalore 560 034, India

2004

Certificate

This is to certify that the thesis entitled 'Measurement of the Casimir-Polder Force at sub-micron distance scales using an atomic beam' submitted to the Bangalore University by Mr. D. Suresh for the award of the degree of Doctor of Philosophy in the faculty of Science, is based on the results of the investigations carried out by him under my supervision and guidance, at the Indian Institute of Astrophysics, Bangalore. This thesis has not been submitted for the award of any degree, diploma, associateship, fellowship etc. of any university or institute.

Indian Institute of Astrophysics,
Bangalore
May, 2004

Prof. R Cowsik
(Thesis Supervisor)

Declaration

I hereby declare that the matter contained in this thesis is the result of investigations carried out by me at the Indian Institute of Astrophysics, Bangalore, under the supervision of Prof. R. Cowsik. This work has not been submitted for the award of any degree, diploma, associateship, fellowship etc. of any university or institute.

Prof. R. Cowsik
(Thesis Supervisor)

D. Suresh
(Ph.D. Candidate)

Indian Institute of Astrophysics
Bangalore 560 034, India
May, 2004

Acknowledgements

This experiment was already underway when I joined the effort. The laboratory was just beginning to take shape. The many areas of expertise required to do an experiment at the edge of known technology placed many technical demands upon us. Much of what was needed was all but unknown to many of us. When I now turn and look back upon that time, when we so naively believed this to be a 'simple' experiment, I am more than amazed at our audacity. Were it not for many fine people who have helped us over these years of growth, neither this experiment nor the laboratory would have ever have come into existence. No words of thanks can adequately express my gratitude for their aid through all these difficult years.

Prof.R.Cowsik, my thesis supervisor had, with his far sighted vision, foreseen the importance of these experiments. I am grateful to him for his steadfast support and for his guidance.

The support of many people at the Indian Institute of Astrophysics has been crucial for the success of this effort. It has always been a pleasant surprise to learn how wholeheartedly they are willing to throw their shoulder to the wheel when our rickety vehicle got stuck in the proverbial pothole. To all of them I would like to express my everlasting gratitude.

There was many a time when I had all but given up in despair. When the effort seemed all too beyond our meagre means. Were it not for my colleagues Unni and Raji whose spirits could never be dampened, I would, I am sure, have quit long before this. It has been a pleasure working with them, sharing the joys and sorrows of building an apparatus. And somewhere in the background has always been Krishnan whose insight and support were something I have fallen back on, time and again.

My fellow graduate students in the institute know well my propensity for getting into trouble, for they have always been there to pull me out of it. I have been fortunate to have their cheerful support and encouragement. I would like to thank them for their stimulating company and many merry evenings.

There have been so many little things which I have learnt from so many different people. Often it is the un-noticed, chance encounter with a small trader in electronic

items, a technician passing through the laboratory, a salesman or an engineer in a factory who has become my teacher. Many of them have gone beyond the call of their duty to enthusiastically support our dreams and feel the thrill of this adventure. To them too I would like to express my thanks.

My brothers and sisters, my wife and daughter who have so valiantly borne with me through these many years, who have made their interests second to my own and yet have put up with my many failings I cannot adequately express my gratitude. Were it not for their steadfast faith in me I would have indeed lost faith in myself.

To the memory of my parents, who had sacrificed the energy of their youth and the comfort of their old age for the happiness and education of their children, I dedicate this thesis.

Preface

This thesis describes an effort wherein we have developed a versatile atomic beam apparatus. The objective is to study the Casimir-Polder interaction of the atoms with surfaces. The apparatus is capable of measuring isotopic abundances in the atomic beam and can therefore probe the differences in the responses of various isotopes. Study of these interactions has gained significance in recent times because Casimir interactions constitute the dominant background in any measurement of gravitation at distances less than 1 mm. An accurate measurement of these forces gives rise to stringent limits on the strength and distance scale of new forces postulated in theoretical attempts to unify gravity with the standard model of particle physics. The Casimir-polder force is interesting from another point of view as well. It is a fully quantum electrodynamical effect with the added attraction of being measurable at macroscopic distances of several microns.

We describe here the construction and operation of an apparatus which was, but recently, completed and present some preliminary observations of transmission through cavities about 10 μm in width. We also give a brief review of similar experiments aimed at furthering our understanding of atom-surface interactions. At the end, we indicate possible future directions in this pursuit.

CONTENTS

1. A BRIEF INTRODUCTION TO OUR STUDY OF THE CASIMIR-POLDER FORCES

Abstract

In this chapter we recount briefly the history of the study of Casimir-Polder forces with a particular emphasis on the recent interest in the field. We note that even though the presence of this remarkable manifestation of the quantized electromagnetic vacuum is well established, there still remain many features which motivate our experiments. Among these, the most interesting is perhaps related to the efficacy of such experiments to probe new interactions, predicted by theories that go beyond the Standard Model of particle physics. We describe the design strategy of the apparatus that we have built and assess its sensitivity for the detection of such interactions. We end the chapter giving an overview of the organization of the thesis.

1.1 Introduction

The attraction of neutral atoms to each other and to metallic surfaces was well known even during the 19th century. It was known that this force had a range much shorter than that of the forces between charges studied by Coulomb and the forces of gravity between masses, presented in the Principia of Newton and studied by Cavendish. Since that time, a detailed understanding of these forces has been achieved through the efforts of a large number of scientists including Laplace, Gauss, van der Waals, Maxwell, London, Lennard-Jones, Casimir, Polder and Lifshitz. These forces play an important role in adhesion, microbiological interactions, adsorption of gases and the operation of the Atomic Force Microscope and microelectronic devices.

There are many excellent reviews ([13],[19],[16] and references there in), which

trace the development of the field systematically, from before the formulation of Quantum Mechanics to modern times where the theoretical analysis makes full use of the language of Quantum Electrodynamics. Similarly, the reviews also treat the experimental developments in detail, from early observations of surface-tension and the deviations from the laws of an ideal gas, to the most recent experiments in 'Cavity QED'. We will confine ourselves here to a brief presentation of the salient aspects of the Casimir-Polder forces, only in so far as these have motivated us to build a versatile apparatus for the study of these and similar forces.

It was made clear by the analysis of London, based on Classical Electrodynamics that the force between a 'neutral' atom and a conducting surface, for example, was due to the interaction of the static electric dipole moment with its "mirror image". The potential experienced by a static point dipole ($\overrightarrow{p}$) placed at a height z above a flat conducting surface is given by

$$U(z) = -\frac{p_x^2 + p_y^2 + 2p_z^2}{64\pi\epsilon_0 z^3} \tag{1.1}$$

Now, if the atom has no net-dipole moment then the potential $U(z) = 0$, and the force vanishes. Lennard-Jones realized that quantum mechanically, the situation is dramatically different: whereas the expectation value of the dipole moment operator ($\overrightarrow{r}$) may vanish, the expectation value of $U(z)$ does not vanish, as it depends quadratically on ($\overrightarrow{p}$). Let us now suppose that the atom's dipole moment is fluctuating about a mean value of zero, then this fluctuating dipole will induce fluctuating charges on the surface and their mutual interaction will generate the potential,$U_{LJ}(z)$, derived by Lennard-Jones.

$$U_{LJ}(z) = -\frac{\langle 0|p_x^2 + p_y^2 + 2p_z^2|0\rangle}{64\pi\epsilon_0 z^3} \tag{1.2}$$

It was Purcell[23] who first pointed out that in consideration of fluctuating dipoles, say with a frequency ν, a new length scale gets introduced

$$z_0 = \frac{c}{\nu} \tag{1.3}$$

Accordingly, the field retardation effects become significant at $z >> z_0$ and the Lennard-Jones potential will be modified.

Now, how is the fluctuating dipole generated? The fluctuations arise due to the zero point energy of the dipole oscillator, maintained as such by exchanging virtual photons with the fluctuations of the electromagnetic vacuum. The potential for large values of z, derived formally using quantum electrodynamics by Casimir and Polder, is given by

$$U_{CP} = -\frac{3}{32\pi^2\varepsilon_0}\frac{\hbar c\alpha}{z^4} \tag{1.4}$$

where α is the polarisability of the atom in the ground state which may be calculated using perturbation theory to be

$$\alpha = \frac{2e^2}{3}\sum_{n=1}\frac{\langle 0|\overrightarrow{r_e}|0\rangle}{E_n - E_0} \tag{1.5}$$

Here E_n is the energy of the various excited states of the atom which can be reached from the ground state of energy E_0, through dipole transitions. The Casimir-Polder effect may be understood along lines similar to those employed by Bethe to analyse the Lamb shift in atomic energy levels. Bethe proposed that the Lamb shift is a consequence of the emission and absorption of virtual photons from the vacuum field. While both effects arise due to similar causes, Casimir-Polder effect has the added interest that it is manifest even at macroscopic distances of the order of micron. In pursuing the analogy to the Lamb-shift in making a formal calculation of the Casimir-Polder potential, Aspect and Dalibard [6] point out that one should correctly take into account, the modification of the allowed modes of the quantum vacuum by the presence of the conducting boundary. The force of attraction between two conducting plates due to this very same cause had been calculated by Casimir, and is called the Casimir effect.

Lifshitz developed a comprehensive theory of the interaction between an atom and a semi-infinite body characterized by a linear susceptibility $\epsilon(\omega)$. This theory is fully capable of discussing the Casimir-Polder and the Casimir effects in the case

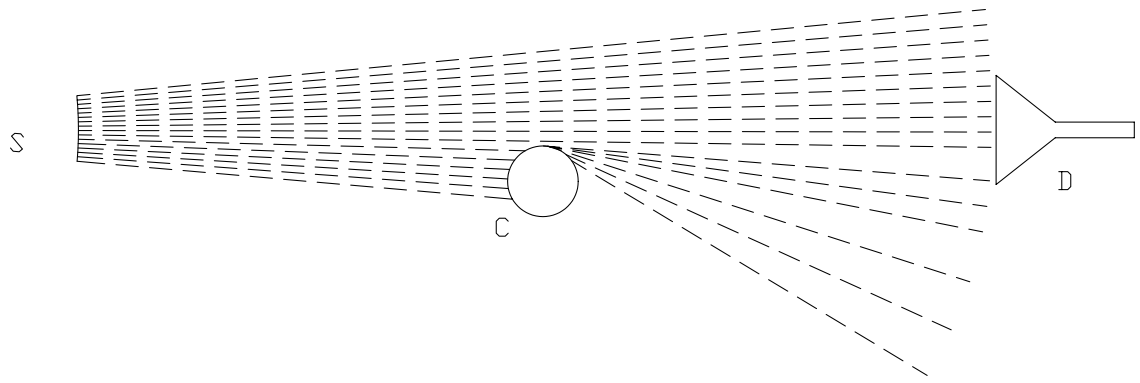

Fig. 1.1: Experimental concept for detection of the Lennard-Jones potential

of dielectrics and surfaces of finite conductivity. The Casimir-Polder potential for $z \gg z_0$ given by Lifshitz theory is

$$U_{CPL} = -\frac{3}{32\pi^2\varepsilon_0}\,\frac{\hbar c\alpha}{z^4}\,\frac{\epsilon(\omega_d)-1}{\epsilon(\omega_d)+1}\,\Phi(\epsilon) \tag{1.6}$$

where $\phi(\epsilon)$ is a slowly varying function of ϵ of the order of unity, $\epsilon(\omega_d)$ is the susceptibility evaluated or measured at the frequency ω_d from an energy level at $\hbar\omega_d$ above the ground state making the dominant contribution.

1.2 Experimental Strategy

Postponing a review of the various experiments which have established the presence of atom-wall interactions both in the Lenard-Jones and in the Casimir-Polder domains we now focus on the broad strategy adopted in these experiments. As the atom approaches very close to the surface of a conductor at distances

$$z \ll z_0 \approx \frac{2\pi c}{\omega_d} \tag{1.7}$$

The force increases as z^{-4}:

$$F_{LJ} = -\frac{\partial U_{LJ}}{\partial z} = \frac{3U_{LJ}}{z} \sim z^{-4} \tag{1.8}$$

The basic idea of the experiment is illustrated in the Fig. 1.1

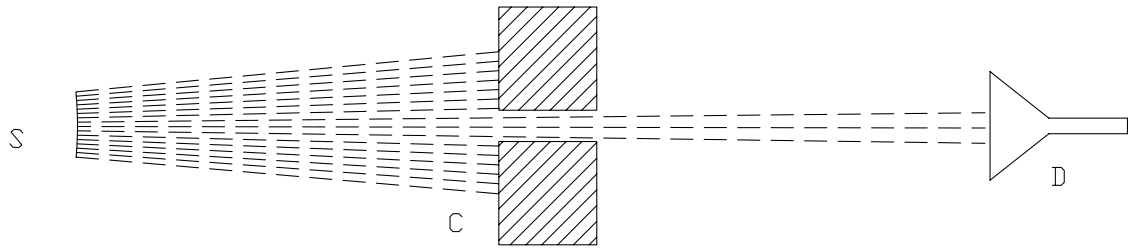

Fig. 1.2: Improved experimental concept for the detection of the Casimir-Polder forces

A narrow beam of atoms or molecules emanates from a source of small linear dimensions. A detector D placed some distance away is capable of detecting the beam. A cylinder made of a good conductor and having a highly polished surface is slowly moved up, progressively intercepting the beam. The atoms arriving at grazing incidence suffer a deflection due to the Lenard-Jones force and the changing count-rate in the detector is recorded and analyzed to yield the potential U_{LJ}. With this method Raskin and Kusch[7] could establish the presence of the Lenard-Jones potential.

As the impact parameter of the atoms with the surface increased, the force decreased rapidly, initially as z^{-4} and even more rapidly as z^{-5} in the Casimir-Polder domain with $z \gg z_d$. Accordingly their experiment could not study the long-range behaviour of the forces. The reasons behind this are several, notably the following: a) The atom beam detected by the detector always had a large range of impact parameters, making it difficult to analyze the count rate-distance curve to establish the behavior of the forces specifically at the large impact parameter domain. b) A large background flux of atoms was always present, further reducing the sensitivity of the experiment.

A group of researchers at York University, studying the cavity QED effects on atomic transitions developed an improved technique. The concept underlying this is sketched in Fig. 1.2

We have, here, as before a source S which generates a narrow beam of atoms. A narrow channel C formed out of a highly conducting material intercepts the beam (instead of the cylinder as in the previous design). The atoms must successfully traverse the channel in order to be detected by the detector, D. The atoms that hit

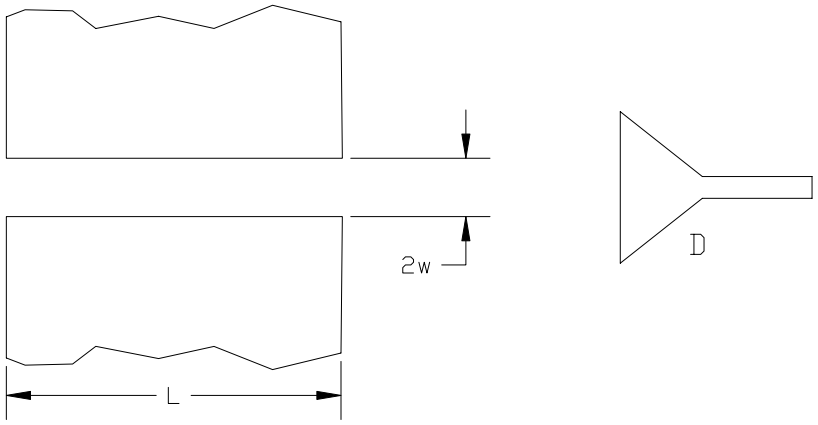

Fig. 1.3: A sketch showing the dimensions of the cavity for assessing the sensitivity of the experimental scheme; L=length of the channel, 2w=width of the channel.

the sides of the channel during their traversal either get adsorbed or get scattered at large angles with respect to the beam. In either case they contribute negligibly to the count rate in the detector. Clearly, this design has several advantages and these are listed below:

a) The beam traversing the channel has a well-defined range of impact parameters.

b) The detector essentially detects the traversed beam and beam intercepted by the sides of the channel and those which go and hit outside the entrance aperture do not contribute significantly to the background count rate.

c) The channel spacing could be modulated, thereby changing the range of impact parameters accepted by the detector. Alternately, it is possible to vary the length of the channel, thereby increasing the time interval over which the traversing atomic beam is subjected to the influence of the forces.

In this design the forces tend to attract the atoms to the surface and thus reduce the phase-space of the transmitted beam with respect to that expected solely due to the geometric aperture of the channel. The degree of observed depletion in the flux with respect to the flux expected for the geometric aperture, or simply the opacity of the channel, constitutes the signal. The sensitivity of this experiment may be estimated (for purposes design) as given below:

The flux expected, f_g, through a channel of length L, and width $2w$ (see Fig. 1.3) is proportional to the area solid angle product of the channel and may therefore be expressed as

$$f_g = f_0 \, \frac{4w^2}{L^2} \tag{1.9}$$

Now, let us assume that in the presence of a force the geometric aperture is reduced so that the effective area-solid-angle is written as

$$f_e = f_0 \, (1 - \eta) \tag{1.10}$$

where η is the opacity of the channel. It is convenient to parametrise eq.1.10 in parallel with eg.1.9 as

$$f_e = f_0 \, (1 - \eta) \equiv f_0 \frac{4(w - \delta)^2}{L^2} \tag{1.11}$$

where δ is a phenomenological length parameter which reduces the effective width of the channel. Qualitatively, δ represents the nearest distance up to which an atom may approach the wall without being attracted so strongly that it hits the surface. Assuming that $\delta \ll w$, Eqns. 1.9, 1.10, 1.11 yield

$$\delta = \frac{\eta w}{2} \tag{1.12}$$

Now let F be the force acting on an atom as it traverses the channel; this force acts for a duration of $\triangle t = \frac{L}{v}$ where v is the velocity of the atom. The deflection suffered by the atom is given by

$$\triangle\theta = F \cdot \triangle t \cdot \frac{1}{mv} = \frac{F \; L}{mv^2} \approx \frac{F \; L}{k_B T} \tag{1.13}$$

Here m is the mass of the atom and T is the temperature of the source of atoms. Now we may approximately set the minimum detectable angle in the experiment to be

$$\triangle\theta_m = \frac{\delta}{L} = \frac{\eta w}{2L} \tag{1.14}$$

Equating $\triangle\theta$ and $\triangle\theta_m$ we may find the minimum detectable force (F_m)to be

$$F_m = \frac{\eta k_B T w}{2L^2} \tag{1.15}$$

For typical values $\eta = 10^{-3}$, $T = 300$ K, $w = 10^{-3}$ cm and $L = 1$ cm, F_m turns out to be $\sim 6 \times 10^{-24}$ Newtons. We now return to the expression of the Casimir-Polder force on an atom and present the formula in convenient units.

$$F_{CP} = -\frac{6 \times 10^{-26}}{z_\mu^5} \quad \text{Newtons} \tag{1.16}$$

Here z_μ is the distance of the atom from the conducting surface in microns. Comparing this with the estimate of sensitivity of measurement given in Eqn. 1.16 one notes that the Casimir-Polder force may be measured up to a distance of ~ 0.4 μm.

It is important to note right away here, that the actual performance of this experiment poses great challenges:
a) The alignment of the atomic beam with the cavity has to be achieved to ~ 100 micro-radian accuracy, with a stability of similar value through out the experiment. This requires extraordinary skills and procedures to implement, especially within a ultra-high vacuum system.
b) The geometric area-solid angle product of the channel is very small, so that even with intense atomic beams the throughput is rather small. Further, more intense the beam, higher is the background generated by the stray atoms.
c) The technical problems of modulating the channel spacing w are considerable, especially in the inaccessible regions of an ultra-high vacuum system.

The difficulties were overcome and the stringent technical requirements were met for the first time through the pioneering efforts of Hinds, Haroche, Sandoghdar and Sukenik, at the Yale University. We will return to a description of their remarkable experiment later. But here, we wish to focus attention on the high sensitivity of their design, and discuss possible application of this scheme for the search of other feeble forces with possible ranges extending from ~ 100 nm to ~ 100 μm.

1.3 New feeble forces beyond the Standard Model

We now briefly digress and summarise some of the ideas in high energy physics and cosmology which motivate a broad class of experimental investigations of the kind undertaken here. Extensive and elegant discussions of the physics and cosmology underlying these studies are given by Adelberger et al. [1], Fishbach and Talmadge [12], Long et al. [17] and Mostepanenko and Trunov [22]. The essential ideas stem surprisingly from the extraordinary success of the Standard Model. Not a single experiment carried out with particles accelerated to high energies has indicated any contradiction with the predictions, how so ever faint. Indeed every prediction of the model has been confirmed by the experiments. Thus it is very tempting to include gravitation within its purview in a grand unified scheme. But this has proved very difficult, probably because of the very faintness of gravitation. For example, the force between two electrons is $\sim 10^{-42}$ of the Coulomb attraction between an electron and a positron at macroscopic distances. Another way of stating this is that using the Newtonian constant of gravity we can define a Planck mass

$$M_{Pl} = \sqrt{\frac{\hbar c}{G}} \sim 1.2 \times 10^{19} GeV/c^2 \tag{1.17}$$

This is much larger than the 300Gev associated with electroweak unification, this large difference in energy scales is referred to as the "Hierarchy problem". Conventionally the hierarchy problem has been ameliorated with the ideas of Super-symmetry and more recently in String-theories and M-theories by postulating extra dimensions. These theoretical ideas taken in conjunction with a variety of experiments indicate the presence of bosons of low mass mediating Yukawa-like forces at sub millimeter distances. As emphasised by Moody and Wilczek, about 20 years ago, some of these may generate spin dependent forces. The measurement scheme perfected by Hinds and collaborators may be able to probe a parameter domain more sensitively than some of the ongoing experimental searches for these new hypothetical forces.

Work carried out in cosmology first with supernova of type 1a as the probe initially, and with other probes such as the fluctuations in the universal microwave background

subsequently, have brought out the rather astonishing and disquieting fact that the Universe is in a state of accelerated expansion. A straightforward implication of this finding is that about 65% of the energy density in the Universe is made up some field that exerts negative pressure. It is well known that quantum-vacuum has this property or indeed the Λ term that may be introduced into Einstein's field equations. This explanation poses several fundamental questions: A simple calculation of the energy density of the vacuum field, even with the introduction of the most severe infrared and ultraviolet cut-off is given by

$$\int_{w_1}^{w_2} \frac{\hbar\omega^3}{2\pi^2 c^3} d\omega = \frac{\hbar}{8\pi^2 c^3}(w_z^4 - w_1^4) \tag{1.18}$$

and has a value 10^{14} times larger than the required value of $\sim$ 10 keV even for a limited range from 400 nm to 800 nm for the domain of integration. Actually one may wish to integrate right up to the Planck-scale, immeasurably exacerbating the problem. A possible avenue for taming these divergences might be Supersymmetry with fermionic fields cancelling out more or less precisely the contribution of the bosonic fields. But why are these cancellations just right to leave behind nearly the critical density we need and why precisely at this epoch of the Universe. The general thinking is that the questions of grand unification and the cosmological issues are intimately related. All the theoretical ideas developed to resolve these issues invariably predict new particles and more to the point new bosons mediating new fundamental forces.

1.4 Design-concepts of our apparatus

Our apparatus follows closely the design developed by Hinds and his collaborators, and incorporates all the advantages of their design. There are a few additional features which make our scheme interesting. Instead of resonant excitation by two superimposed laser beams followed by field ionization, we use conventional electron impact ionization which is indeed a part of a standard residual gas analyzer (RGA) used extensively for characterising vacuum systems. This has the advantage that any atom may be detected by it. We are not restricted to operate the apparatus with a

single atomic species at a time for which the laser frequencies are specifically tuned. Further more, the quadrupole analyzer in the RGA provides the isotopic information on the detected atoms. Thus with our detection scheme a beam consisting of several atomic species may be studied simultaneously and the isotopic composition of each may be determined. The advantages of such a scheme are several, as noted below:

(a) Since the 'signal' in the apparatus is the opacity which is the ratio of the transmitted intensity with respect to that expected solely from geometrical considerations, much of the uncertainties in the experimentation may be eliminated by taking the ratios of the transmission of various species with respect to a standard, say He-atoms with low polarizability. The transmission of He would be close to geometric and if necessary, a small correction may be applied to it.
(b) Many atomic species may be studied simultaneously.
(c) Keeping in mind the capability of the mass-spectrometer to resolve isotopes we have chosen xenon as the primary system to study. The isotopic abundances of the 9-isotopes of xenon, taken from IUPAC is reproduced in Fig. 1.4.

The large number of isotopes of Xe, especially with even-even and even-odd proton-neutron numbers makes it an interesting system to study, with the added advantage that one of these isotopes may be used as an internal calibrator. ^{129}Xe and ^{131}Xe have nuclear magnetic moments of $^{129}\mu = -0.77686$ and $^{131}\mu = +0.69066$ respectively. These features allow the study of the possible effects of hyperfine interaction on the Casimir-Polder forces. Also the isotope-set provides a sequence of nuclear isospins and three different spins which allows us to search for forces which may couple the these as well.
(d) The elemental abundance of Xenon in air is very low; thus we expect that residual gas, degassing from the walls and leaks will contribute negligibly to the background.

In our apparatus there are four regions where the Xenon atoms might interact closely with the walls of channels: (1) An array of capillaries made of ceramic material, of diameter, $d = 2w = 12.5$ μm and length, $L =$ 0.05 cm. (2) A metallic channel of

Atomic Weights and Isotopic Compositions for Xenon				
Isotope	RelativeAtomic Mass	Isotopic Composition	Spin	Magnetic Moment
	atomic mass units	%		Nuclear Magneton
124	123.905 8958(21)	0.09(1)	0	
126	125.904 269(7)	0.09(1)	0	
128	127.903 5304(15)	1.92(3)	0	
129	128.904 779 5(9)	26.44(24)	1/2	-0.7768
130	129.903 5079(10)	4.08(2)	0	
131	130.905 0819(10)	21.18(3)	3/2	0.69006
132	131.904 1545(12)	26.89(6)	0	
134	133.905 394 5(9)	10.44(10)	0	
136	135.907 220(8)	8.87(16)	0	

Fig. 1.4: Isotopic compositions of Xe as reported by NIST.

width 200 μm and length, $L = 2$ cm. (3) A wedge shaped channel, similar to the one set-up by the Yale group. (4) A second metallic channel similar to item (2). These provide a variety of conveniences, as presented later in the thesis.

1.5 Overview of the material covered in chapters II, III, IV, and V

In the Chapter 2 we describe the instrument completely, including the procedure we adopted in the fabrication of various components (as also our trials and tribulations). The alignment of the various sub-systems posed the greatest challenge and we describe our method of alignment, as also the tests we conducted in-situ, that the system stayed in alignment during pump-down etc. The data acquisition and control software that we developed to operate the rather complex apparatus are also described. In our view this chapter forms the core of the thesis.

Chapter 3 is devoted to the presentation of the procedure adopted for the study and preliminary data acquired for characterising the apparatus. We also describe in detail the various procedures for the normalization of the signals and the subtraction

of the various backgrounds.

In Chapter 4 we analyse the data, preliminary as they might be, and draw tentative conclusions regarding the Casimir-Polder force and other forces which are posited by modern theories of elementary particles.

Finally in Chapter 5 we briefly summarize what is known experimentally about Casimir-Polder forces, where the conflicting evidence lies and what experiments we would like to carry out using the apparatus we have built to address some of the outstanding issues.

2. DESCRIPTION OF THE APPARATUS

Abstract

In this chapter the experimental apparatus that has been developed to measure the Casimir-Polder force and any of the feeble forces recently posited in extensions of the standard model, will be described in detail. The experiment involves detecting the isotopic composition of an atomic beam and the changes in its composition when it interacts with a pair of electrically conducting surfaces. A vacuum chamber with differential pumping was developed to generate a dense well-collimated atomic beam with low background gas density. A pair of gold coated glass surfaces, held a few microns apart, were introduced into the atomic beam and were aligned parallel to the beam axis. The gap between the surfaces and their orientation could be adjusted from outside the vacuum chamber. The atoms that were transmitted through the gap were mass-resolved and counted using a quadrupole mass-spectrometer and a photon-counter. The control and data acquisition in the experiment was through a PC interfaced to the various actuators and instruments.

2.1 Introduction

Study of atoms in the proximity of surfaces has been an active area of research for many decades. However, with the realisation that the modification of the modes of the vacuum electric field near a conducting surface [5] had observable consequences on the radiative properties of atoms, led to a resurgence of both theoretical and experimental efforts in this area. The first observation of altered spectra in atoms near surfaces was by Drexhage[10] who observed fluorescence of dye molecules placed near a surface. The forces that arise due to these distance dependant interactions were

also observed as deflections of atoms from ballistic trajectories when they fly past a surface. Shih et al. [27] observed deflection of a beam of cesium atoms due to its interaction with gold and glass surfaces. They measured atomic beam flux as a function of distance into the geometric shadow of the surface. Their efforts showed the existence of Lennard-Jones interaction between the atoms and the surfaces. Their data also showed that the Lennard-Jones potential accounted a major portion (85%) of the observed interaction but they were not able to confirm the contribution of the "instantaneous dipole fluctuations" [26]. Sukenik et.al [31] measured the flux of ground state Na atoms through a narrow channel as a function of its width. They observed a decrease in the transmission of these atoms through the channel as a function of its width. The width of the channel was in the range of 0.6 μm to 10 μm. The beam was generated from a heated oven acting as a reservoir and a 10 μm slit as the collimating element. The atoms emerging through the slit were incident upon a two gold coated glass surfaces which formed a narrow wedge. The atoms passed through this wedge and were detected by a channel electron multiplier after ionisation. Sukenik et al. were able to establish that at distances larger than 0.6 μm the interaction potential between atom and the conducting walls was well described by the Casimir-Polder potential.

Our primary objective was to measure the transmission of a beam of xenon atoms through a gap between two conducting surfaces as a function of the width of the gap. We also wished to measure the transmission of the various isotopes of xenon. In order to maximise this signal many strategies were adopted in the apparatus. The first was to design a source which could generate an intense beam of xenon atoms without increasing the partial pressure of Xe in the detection zone. To keep the background density of xenon low a three stage differentially pumped vacuum chamber was introduced along the path of the beam. The conducting surfaces were a pair of gold coated, optically polished glass blocks. The blocks were held in a suitable mount such that the gold coated surfaces formed a thin wedge. This wedge was positioned in the path of the beam by using vacuum compatible tilt and translation stages. Xenon being a

noble gas cannot be photo-excited to a Rydberg level by any currently available laser. Therefore electron impact ionisation was the favoured route for detection. However electron impact ionisation does not allow us to preferentially ionise the xenon atoms. Therefore the ions were mass-filtered so that atoms from the residual gases in the chamber do not reach the detector. We also added a small amount of helium to the xenon beam so that we had an in-situ calibration of the transmission of the gap. Since the polarizability of helium is about 20 times smaller than that of xenon it approximates the geometric transmission of the cavity. In the following sections these various components of the apparatus (the source, the collimator, the differentially pumped vacuum chamber, the conducting surfaces and the mass-spectrometer) are described in greater detail.

2.2 The Vacuum System

2.2.1 The source

The objective is to generate an atomic beam of high intensity such that its contribution to the background gas density is minimised. An atomic or a molecular beam is created by permitting gas to flow into vacuum through a narrow tube, such as a capillary with diameter, d, much smaller than its length, l. We confine ourselves to the regime of flow where the mean-free-path, λ, of the gas exiting the tube is greater than the diameter of the tube. Such a flow is said to be molecular, that is, atoms follow ballistic trajectories after exiting from the tube. The beam intensity, net throughput and profile depend upon the pressure on the input side of the capillary, the capillary dimensions and, to a smaller extent, on other factors like the temperature, mass and diameter of the atoms or molecules comprising the beam. The following expressions for the intensity, I in atoms s^{-1} $sterad^{-1}$, net throughput, Q in atoms s^{-1}, and beam half angle, H in degrees, are given below[20],

$$I = 1.69 \times 10^{20} \left(\frac{T}{295M}\right)^{\frac{1}{2}} \sqrt{\frac{P}{l\sigma^2}}\ d^2 \tag{2.1}$$

$$Q = 2.16 \times 10^{21} \left(\frac{T}{295M}\right)^{\frac{1}{2}} \frac{d^3}{l}\ P \tag{2.2}$$

$$H = 2.48 \times 10^2 \sqrt{Pl\sigma^2} \tag{2.3}$$

Here T is the absolute temperature and P the pressure of the gas behind the capillary in Torr, M is its molecular weight and σ is the molecular diameter in Angstroms. These equations apply when the pressure P is such that $d < \lambda < l$, where $\lambda \approx \frac{5\times10^{-3}}{P}$ cm, (P in Torr).

As can be seen from the expressions above, it is advantageous to choose capillaries of small $\frac{d}{l}$ ratio in order to obtain narrow beams. However this would also reduce the axial intensity. The solution is to use an array of capillaries instead of single one. In which case the beam half angle,H, does not change but the beam intensity increases linearly with the number of capillaries(b) and the ratio of beam to background density increases as $\sqrt{b}$ [29].

The optimal operating pressure P is decided by the condition $d < \lambda < l$. However given the limitations of pumping speed available on the exit side of the array we must maintain the net throughput of the array such that the mean free path of the background gas in this area is several times larger than the chamber dimensions.

To maintain a constant beam flux, the pressure on the input side of the capillary needs to be maintained constant. A reservoir of the desired gas was attached on the input side and as the gas flowed out of the reservoir it had to be replenished in order to maintain a constant pressure. The steady-state pressure in the reservoir could be adjusted by using a leak valve on the gas input line. Xenon being an expensive gas the initial trials of the apparatus were carried out with a mixture of helium, neon and argon in 6:47:47 ratio. In addition to this there were also separate Xe and He

cylinders. To control the partial pressures of various gasses in the source, a system of tubing with Swagelok fittings and valves was put together. Each gas line, from cylinder to source, included a leak valve and an on/off valve in series. These allowed us to control the flow rate of various gasses into the reservoir. While the leakvalves on the Xe and He-Ne-Ar mixture lines was adjustable, the valve on the He line was a constant calibrated leak. The partial pressure of He as maintained by this constant leak, later turned out to be insufficient and we used a separate purging line to add helium to the reservoir. However there was no leak valve on this line, so flow-control was done by carefully adjusting an on/off ball valve. This system allowed a desired gas mixture to be filled into the reservoir. The actual procedure followed to obtain an optimal mixture is described in section 3.3.

The 'reservoir' in our case was a six-way CF35 cross which was pumped by a rotary-vane pump. The pumping port could be valved off, if needed, by an inline vacuum valve. A gas inlet valve was located on the opposite arm. Both were bakeable to 200 deg.C. The capillary array was mounted on a CF35 to CF63 reducer flange and attached to one of the arms of the six-way cross along the axis of the apparatus. A viewport was mounted inline with the array for alignment purposes. The capillary array was a regular hexagonal array (see Fig. 2.1)of capillaries which were about 12.5 μm in diameter and 500 μm long. A circular area on the array, five millimeters in diameter, was exposed for transmission of atoms from the reservoir. A Varian Convectorr gaugehead monitored the pressure in the reservoir (the pressure, P, on the entry side of the capillary).

2.2.2 Collimation Chamber

The reservoir was attached to a collimation chamber through a flexible bellows. This bellows allowed the source to be translated and rotated with respect to the collimation chamber. This freedom was required to align the source (and hence the beam axis) with the various collimating elements in the apparatus. A CF63 gate valve (No.1) was incorporated between the bellows and the capillary array. This gate valve, when

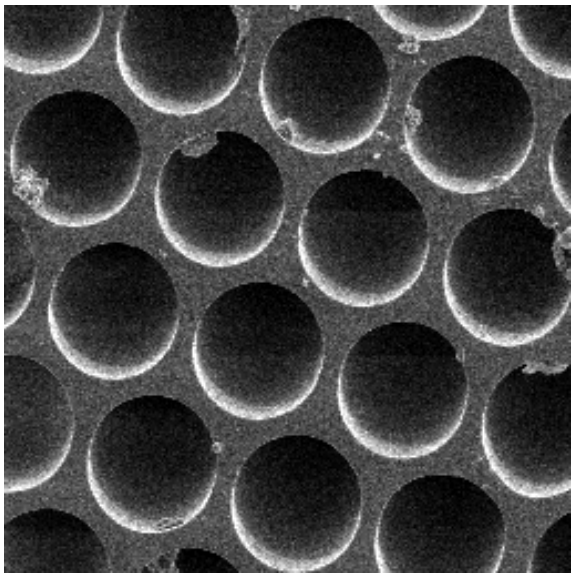

Fig. 2.1: A scanning electron microscope image of the capillary array showing the regular hexagonal array of capillaries each 12.5 μm in diameter. Gas from the reservoir effusing through these 500 μm long capillaries forms the primary atomic beam which is further collimated using narrow slits.

shut, could completely isolate the collimation chamber from the atomic beam. This is a useful feature in leak testing and troubleshooting the system. The collimation chamber was a CF100 six-way cross, pumped by a 500 l/s Pfeiffer turbomolecular pump (model TMU 521). The beam, after emerging from the capillary array, was incident on a narrow rectangular channel (see Fig. 2.6) located, about 50 cm away, on the opposite side of the collimation chamber. The channel was a 1 cm long, 200 μm wide slit cut into a 20 mm thick stainless steel block. The slit allowed only the axial portions of the beam, which were of high intensity, to pass through and posed a high impedance to the background gas in the chamber. This gas being enriched with atoms from the beam, would have caused a large background signal at the detector. The pressure in the reservoir was adjusted such that the pressure in the collimation chamber was $\sim 1.5 \times 10^{-5}$ Torr. At this pressure the mean free path of atoms in the collimation chamber was about 330 cm, which was five times the length of the chamber. The portions of the beam which passed through the 200 μm channel entered

another chamber called the *interaction chamber*.

2.2.3 Interaction Chamber

The interaction chamber was a cube, one foot along the edge, with large CF200 ports on the four lateral sides. It also had CF100 ports on the top and bottom. This was pumped by another 500 l/s Pfeiffer turbomolecular pump (model TMU 520). The beam, upon entering this chamber, would fall on a gap between two glass blocks. The beam atoms, which scattered off the sides of the glass plates, would add to the general background density and will be detected along with the atoms which passed through the gap between the conducting plates. To prevent these atoms from reaching the detector it was removed into a separate chamber called *the detection chamber*. The atoms emerging through the gap between the plates, which have not suffered any collision with the surfaces, will be highly collimated in the transverse direction, since the opening angle in the horizontal plane is $\sim 0.3 \times 10^{-3}$radians. These atoms will therefore pass through into the detection chamber through the second 200 μm slit (Channel 2) which separates the interaction chamber from the detection chamber. However the channel would once again pose an impedance to the flow of the background gas as its conductivity is about 10^{-4} Torr liters per sec. Each high impedance channel thus produces a pressure differential of about four orders of magnitude to the partial pressure of the beamed gas in the chambers. This results in the partial pressure of the species of interest in the detection zone to be less than 10^{-13} Torr. The vacuum system thus acts to discriminate against the scattered gas by imposing a restriction on the acceptance solid angle of the detector besides providing high impedance to the scattered gas atoms.

2.2.4 Detection Chamber

The detection chamber was pumped by a 60 l/s turbomolecular pump from Pfeiffer (Model TMP 071) backed by a diaphragm pump and could be isolated from

the interaction chamber by another CF63 gatevalve (No.2). The chamber reached 5×10^{-10} Torr pressure even when the beam was active indicating that the net throughput from the beam was much smaller than the outgassing from the walls of the chamber. All the chambers in the system (with the exception of the source) were found to reach the base pressure of their respective turbopumps when the beam was shut off by closing the gate valve No.1.

2.3 The Mass Spectrometer

The mass-spectrometer is a residual gas analyser (Model No. RGA200) supplied by the Stanford Research Systems. It was located in the detection chamber facing the beam emerging from the high impedance channel No.2. Its sensitivity of 0.5 amu over a range of 1 to 200 amu allowed us to measure the flux of each isotope separately.

The mass-spectrometer consists of four parts: a) the ioniser b) the mass filter c) detectors and d) the control electronics. It could be remotely controlled through an RS232 link, by a PC running the driver software supplied by the manufacturer. There were also a library of function calls which enabled us to write our own control programs. The ioniser used electron impact ionisation and had a confined space charge of electrons at a mean energy of about 80 eV. This mean energy could be adjusted, over a range of 60 to 105 eV, to maximise ionisation probability of the species of interest. The ions produced in the ioniser were accelerated into the quadrupole mass filter by electrostatic lensing. The extraction electrode which is biased negative also prevents the electrons from reaching the detector and resulting in spurious counts. The mass filter used a quadrupole electric field fluctuating at RF frequencies along with DC bias voltages. For a given set of AC and DC levels only one ionic species of a specific e/m ratio has a stable trajectory through the mass filter and will reach the detectors. Since most of the ions are singly ionised the e/m selection effectively acted as a mass selection. The required AC and DC levels were generated by the

control electronics and as per a pre-calibrated system. The filter's pass band could be centered at a required mass through commands from the PC. The ions which survive the mass filter enter one of the two detectors placed at the end of the RGA. A Faraday Cup placed in line with the axis of the detector was used for detecting ion currents in the excess of 50 femto-amps. For detecting ion currents less than that a Channel Electron Multiplier could be used. This was mounted off-axis in order to prevent the high voltages present on it from affecting the mass filter's operation. The CEM had a gain adjustable from 1 to 2000 and the amplified current could be routed to a sensitive femto-ammeter. However, the sensitivity of the ammeter limited the minimum detectable partial pressure to about 10^{-13} Torr even with the amplification provided by the CEM. We therefore requested Stanford Research Systems for an optional feature which allowed us to take the CEM output and directly feed it into an SR400 dual channel photon counter (also from Stanford Research Systems). The photon counter could then count the individual ions arriving at the detector as long as they produced distinguishable pulses taller than 10 mV separated by more than 3 ns (the dead time of the counter). In this mode the gain of the CEM could be set as high as 10^7 by increasing the bias voltage across it to about 2300 V. The number of pulses counted over a regular interval of time was proportional to the flux of atoms of a definite mass impinging on the ioniser.

2.4 Alignment Procedure for beam collimation

The process of alignment in the apparatus turned out to be a non-trivial task when there are several collimating elements of 200 μm (or smaller) widths. We planned to use the 632 nm He-Ne laser beam(2 mW) as a straight line reference along which we would place the various components. However it was difficult to locate the beam center due to diffraction at the 200 μm slits and the capillary array as well. The matter was further complicated by the fact that the 200 μm slits were actually 20 mm deep channels which gave rise to reflections from the inner surfaces. These reflections made

it more difficult to interpret the observed diffraction patterns. However, we developed a reliable alignment procedure with repeatable results which is described in brief here.

First, the source was decoupled from the bellows and the capillary array was removed. The detector as well as the high impedance paths were similarly dismounted, so that a clear line of sight was available along the axis of the chamber. A green, 543 nm He-Ne laser was positioned on the source side so that its beam traversed along the symmetry axis of the chambers. Of the two high impedance channels one (No.1 in Fig. 2.6) was rigidly located on the Interaction chamber, with no scope of lateral or rotational movement. The laser beam was adjusted with a beam steering apparatus till a symmetric diffraction pattern of the high-impedance slit was obtained on a screen placed at the far end (detector side). This then became the primary reference for the alignment. The second high-impedance slit (No.2) was positioned so that its position and orientation could be adjusted. This was aligned so that the diffraction maximum of the first slit would fall upon it and a second diffraction pattern was obtained on the screen placed on the other side. At this point a second red (632 nm) He-Ne laser was set up and was aligned with another beam steering apparatus such that it counter propagated along exactly the same path as the green laser. Thus a secondary reference line was generated from the primary. The capillary array was then inserted into its mount in the source and the source (still decoupled) was aligned so that the red laser cast a symmetric diffraction pattern on screen placed on the source side. When proper alignment was achieved the two counter propagating lasers were found to trace each other's path good to one millimeter in four meters. At this stage the source was gently slid forward and coupled to the rest of the apparatus. And its position was once again adjusted till the intensities of transmission were maximised and symmetric diffraction patterns were obtained at both ends of the apparatus. At this stage the detector was attached to the rest of the system. However this immediately cut off all further information about alignment since the detector (an opaque object) was necessarily on the axis of the apparatus. Therefore, a 45 deg. beam-bending mirror was introduced into the detection chamber through a bellows-sealed, linear vacuum feedthrough. This allowed a continuous monitoring of the alignment at any stage of

the experiment and it could be retracted out of the way so as to allow the atomic beam to pass unhindered. Both the red and the green He-Ne lasers were mounted onto the table-frame on which the apparatus rested so that there was no relative movement between them even if the table moved on its flexible supports (ref. section 3.2.

2.5 The preparation and positioning of the conducting surfaces

Each of the conducting surfaces constituting the cavity was made of a polished glass substrate coated with gold. Two identical glass blocks of 60 mm ×15 mm ×10 mm size were used and one of the 60 × 15 mm faces on each block was polished till an optically flat surface was obtained. The flatness was better than a 20th part of the wavelength of red He-Ne laser light (632 nm). The opposite face on each block was polished till it was clear so that the fringe patterns formed on the $\lambda/20$ surface could be observed. The other surfaces were left unpolished with a ground glass finish. All edges were bevelled at 45 degrees to 1 mm along the side. The finished blocks were cleaned with distilled water and propanol in an ultrasonic cleaner and were wiped clean with lint free tissue. They were then mounted in a circular stainless steel cells using Torr-seal, a vacuum compatible adhesive. These steel cells were then mounted in a thin-film coating unit and the pressure in the chamber was lowered to 10^{-3} Torr. The substrates were then cleaned by ion bombardment under a gas discharge. The pressure was then lowered to 10^{-6} Torr. Then temperature of the substrate was then raised to about 200 degrees centigrade before evaporated gold was deposited at the rate of five angstroms per second. The pressure in the chamber during deposition was approximately 10^{-4} Torr. The coating was continued until a pre-calibrated thickness was reached such that an optical transmission of approximately 2% was obtained at 632 nm. This transmission allowed us to use optical interferometry to probe the gap between the gold coated surfaces. The glass substrate, steel cell and adhesive were all coated with gold so that a constant electric potential would be ensured across the entire surface. While the deposition was underway the substrate was rotated about

a vertical axis about 20 cm away from the crucible to provide uniformity of coating. This also resulted in the sides of the cell and exposed portions of glass to be coated with gold, thus avoiding exposed patches of dielectric material. In order to avoid pinholes in the coating, the process was completed in two identical steps each depositing half the required thickness of the gold layer. After the first cycle the dust on the coating was brushed away with a jet of air. The rear face of the glass substrate was left uncoated for transparency.

2.5.1 The assembly of the wedge

The assembly of the glass surfaces to form a thin wedge needed extreme care as the gold coating was fragile and if the surfaces were to rub against one another it would expose the dielectric beneath the coating. Care also had to be taken to avoid trapping dust particles between the surfaces as they were brought close to each other. The assembly of the wedge therefore was carried out under clean room conditions. The glass blocks along with their steel cells were placed in a V-block such that the coated surfaces faced each other. An expanded and collimated beam of light (He-Ne 632 nm) was arranged to pass through the wedge so that the fringes (of equal width) formed by the gold surfaces could be observed. A Beryllium-Copper wire of rectangular cross section (9×100 μm) was stretched across the V-block such that the wire passed between the coated glass surfaces about 10 mm from the top edge. The glass plates were moved closer slowly while a jet of clean tetrafluoroethane was blown over the surfaces. After the surfaces came into contact at the bottom (and touched the wire at the top) the screws which held the steel blocks together were gently tightened till parallel horizontal fringes of equal width were obtained in the wedge. The stretched wire was then cut off just outside the glass blocks and the assembled wedge was ready. The thickness of the wedge near the contact line at the bottom was assumed to be zero. As the thickness increased upwards, towards the wire, a total of 30 fringes could be counted thus serving as a check of the distance scale. The steel cells along with the glass blocks now formed a single block. The wedge shaped gap between the plates

is also referred to as a "cavity" or a "channel" in the text.

2.5.2 The Positioning of the wedge in the atomic beam

The assembled wedge was to be placed in the path of the beam such that the beam was incident on the gap between the plates. The wedge was also to be oriented such that the axis of the beam would pass through between the plates in a symmetric fashion thus providing a clear line of sight from the source to the detector through the gap between the conducting surfaces. In order to achieve this positioning two kinds of movements were necessary. The wedge needed to be translated horizontally till the atom beam was incident on it and next, it had to be rotated about a vertical axis (passing through the point of entry of the beam) so that the gold surfaces may be aligned parallel to the axis of the beam. These movements were achieved by the use of a modified 561 series translation stage and a U200-A optical mount both from Newport (see Fig. 2.2). These stages were modified in several ways to render them UHV compatible. First the black anodising of the stages was removed by an electrolytic process. Then all the blind holes were relieved to prevent trapped pockets of air. After that the lubricant on the stages was removed by cleaning them with propanol and a UHV compatible grease (Krytox LVP) was substituted in its place. The micrometer screws were replaced with Picomotors from Newfocus (Model No. 8301V). These vacuum compatible piezo-controlled screws could be operated from outside the vacuum chamber and thus gave us ability to position the wedge in the beam without opening the vacuum chamber.

In order that the atoms may pass through a well defined spacing between the surfaces the atomic beam height was restricted to one millimeter by placing a 1 mm diameter aperture on each of the 200 μm high-impedance slits. The atoms from the source that reached the detector were therefore limited to those that could pass through both these apertures. The portion of the wedge that was relevant at any one time was therefore limited to one millimeter along its length. The variation in the

gap between the surfaces over this one millimeter was 0.3 μm. In order to change the width of the gap the wedge had to be translated vertically along its length. Thus the mean width of the gap could be changed from about 0 to 15 μm by a translation of 50 mm in the vertical direction. However there were two regions in this range that were inaccessible for measurement of transmission. The 0 to 3 μm range and the 8.1 to 9.5 μm ranges were obscured by the mounting screws holding the wedge assembly together. The Be-Cu spacer occupying a height of 100 μm did not pose a serious obstruction. The translation in the vertical direction was provided by a TS-100 V translation stage from Burleigh Instruments. The stage was mounted on a steel right-angle bracket and was designed to parallel transport the wedge in the vertical direction with errors less than 2 μm in 50 mm of travel. The horizontal translation stage mentioned above was mounted on a platform mounted on this stage (refer Fig. 2.2). The actuator for vertical motion was a linear motion feedthrough inserted through the CF100 port on top of the interaction chamber. The wedge could therefore be parallel transported along its length in the vertical direction from outside the vacuum chamber.

To locate the wedge in the atomic beam we first had to translate the wedge horizontally till the beam was incident on it. The fact that the two optically polished blocks were not at the same height turned out to be an advantage at this stage. One block projected above the other by about a millimeter and this projection acted as if it were a single surface. The beam could therefore be progressively obscured from one side by translating the single surface horizontally across it. As the beam was obscured the flux of ions decreased linearly with the translational position. The wedge was then re-positioned at the point where the flux was half of its maximum. After the wedge was located in the beam axis this way it was rotated till the exposed single surface was parallel to the beam. The signature of this parallelism was that once the obscuring edge of the surface was in the geometric shadow of the glass block, the flux did not change with rotation. The wedge was therefore positioned at the point where the flux reached a maximum and remained constant thereafter. This completed the initial alignment of the wedge. It was then raised till the beam was incident at a

desired width of the gap, using the linear feedthrough (measurement of the width of the wedge is described in 3.4. This vertical translation might alter the horizontal position of the wedge by a few microns but would not affect the transmission in a serious way since the incident beam is about 200 μm in width. More significantly it might also alter the angular orientation. Therefore another rotation scan was performed at this location to maximise the transmitted flux. All actuators were thereafter left stationary till the measurement of flux at this location was completed.

2.6 The data acquisition and control

The various instruments in the apparatus were interfaced to a PC through suitable interfaces (the mass spectrometer (RGA200) through an RS232 interface, the picomotor controller and the SR400 counter through GPIB). The pressure gauges had an analog output of 0 to 10 V range which was scaled to the pressure and this voltage was read into the PC through a data acquisition card. A versatile software platform, LabView (ver.6i), was used to integrate these various interfaces and the instruments into one single virtual instrument (VI). This was a software written in LabView which was developed as part of the apparatus. This program used sub-routines (sub-VI) which were supplied as 'LabView Instrument Drivers' by the various vendors from whom we purchased the equipment. The VI initialised the instruments at start-up, set the required parameters in each instrument and collected the atom flux data using the counter. The various movements of the wedge inside the vacuum chamber were also controlled through this VI. The ion-counts returned from the counter were written to the disk along with time-stamps and various other header data. The experiment was largely 'run' from the PC console.

A schematic diagram and a photograph of the apparatus are shown in Fig. 2.3 and Fig. 2.4 respectively.

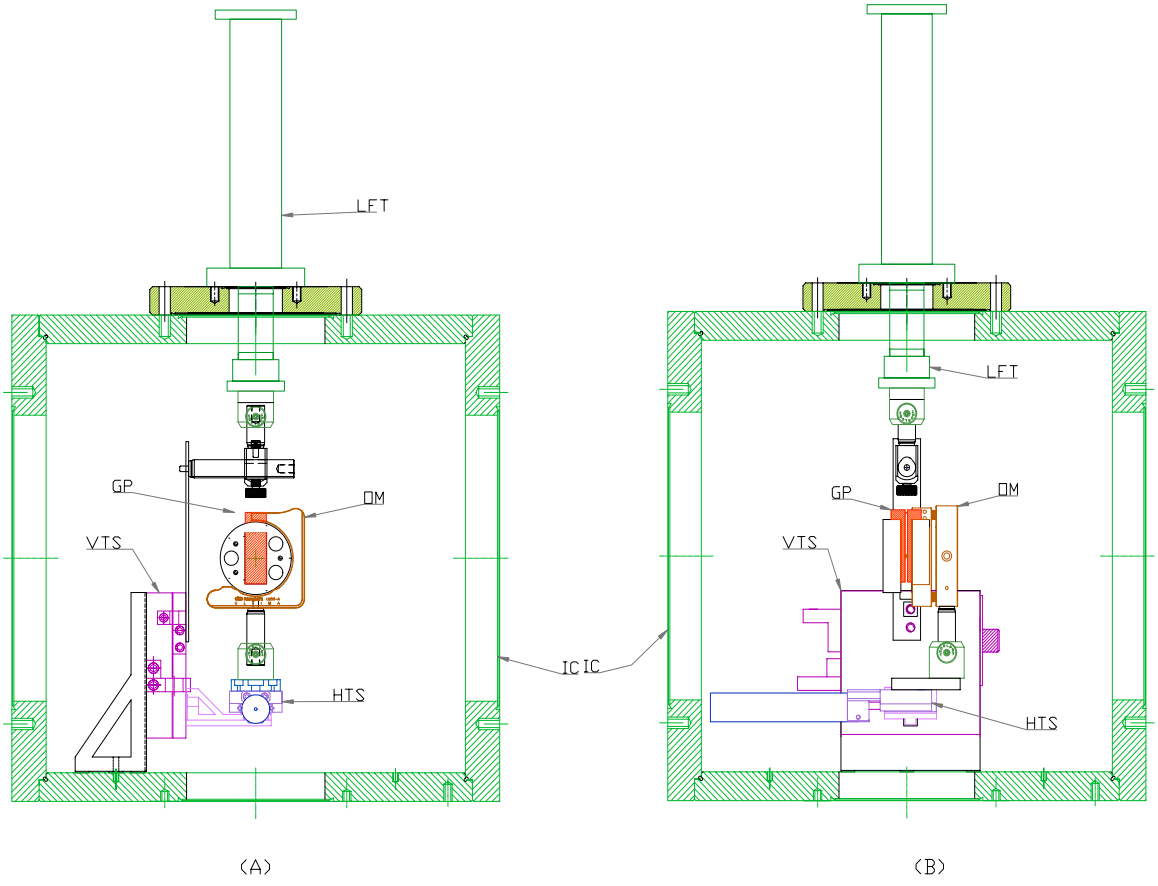

Fig. 2.2: The wedge translation scheme showing the various parts. (A) side-view (B) end-on view looking into the atomic beam. LFT=linear feedthrough, GP=Gold coated plates, OM=Optical mount, VTS=vertical translation stage, HTS=horizontal translation stage, IC= interaction chamber

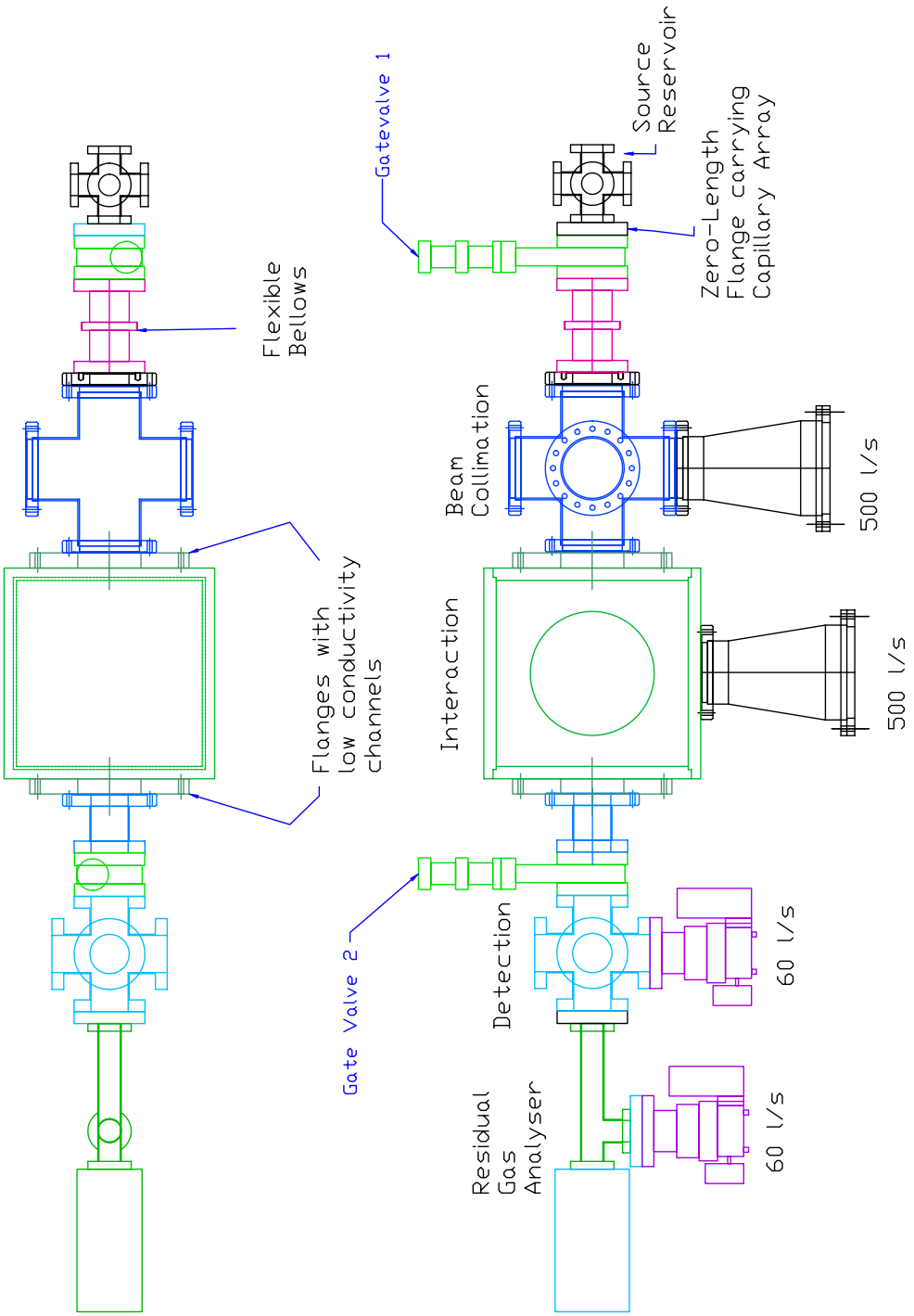

Fig. 2.3: The apparatus with the source followed by three differentially pumped chambers.

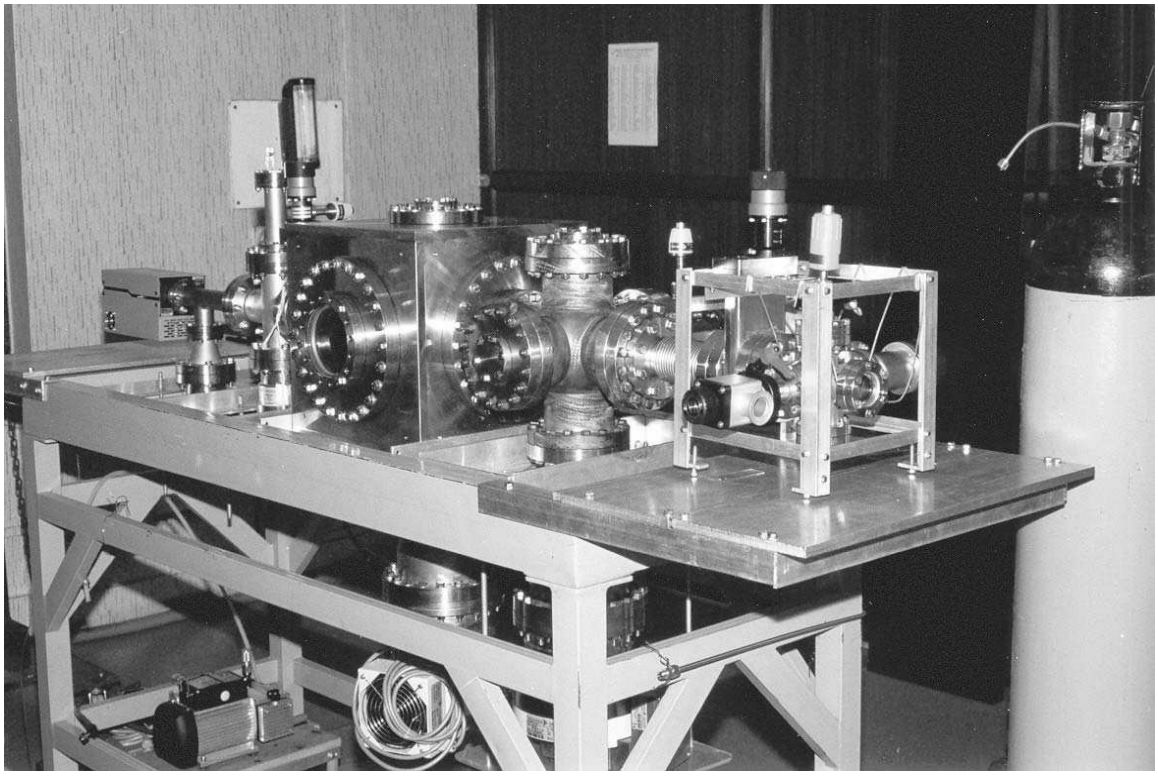

Fig. 2.4: The apparatus showing the four-stage differentially pumped vacuum chamber with the source on the right and the RGA on the left (far end).

3. THE EXPERIMENT

Abstract

In this chapter we describe all the procedures that were followed in setting up and in carrying out the experiment. A laboratory was set up at Bangalore to house the experiment. Various concerns such as dust and vibration isolation were taken into account in the construction of the laboratory. Clean room and UHV practices were followed in the assembly of the apparatus. The mass-spectrometer was characterised and all its parameters were optimised for detection of Xe. The width of the cavity was measured at the position of the atomic beam using optical interferometry. The cavity was aligned to the atomic beam and transmission of several species of atoms was recorded. The data thus obtained was analysed to detect evidence of atom surface interactions. These various steps are described here in detail.

3.1 Introduction

The observation of transmission of atoms through a gap that is a few microns wide requires a clean environment. A typical dust particle can be five microns or larger and such a particle, if present on one of the gold surfaces, can prevent them from approaching each other to sufficiently small distances. Since an interferometric technique is used to measure the width of the gap and various objects have to be positioned with respect to each other to an accuracy of about 10 μm, thermal and vibrational stability are important. The actual collection of data at one cavity spacing takes place takes place over a duration of several hours. The experiment therefore requires stability of incident beam intensity as well as all other parameters over a day or so. Once the vacuum system and various other parts have been assembled the vacuum pumps are

switched on and the pressure in the differentially pumped chambers is lowered over the course of a week. After the base pressures have been reached in all chambers the reservoir is loaded first with Xe and then with He. The pressure in the reservoir and the composition of the gas in it are chosen so as to maximise Xe count-rate. It takes about a day to reach the optimal partial pressure in the chamber. This is a steady state pressure with the gas flowing out through the capillary array being replaced by inflow from the cylinders. The direct beam and background count-rates are monitored over several days to ensure their constancy. Once the system has stabilised the cavity is positioned in the path of the beam as described in section 2.5.2. It is then aligned so that the transmission of He through it is maximised. The count-rate from the background and transmission through the cavity are recorded for several hours. Then the cavity is repositioned at a different spacing and the experiment repeated. The transmission through the cavity of several species of atoms is observed at various cavity widths. The various species are observed in a cyclic manner revisiting the same species every 500 s or so. This is done so that all the species observed in one run have nearly identical conditions. The data thus acquired and its analysis are presented here. The laboratory environment, the manner in which the system was assembled and the procedures that were followed in aligning the apparatus and characterising the detector are explained in detail in the various sections of this chapter.

3.2 The laboratory environment

Recognising the need for a clean laboratory with minimal ground vibration our initial plan was to set up the experiment away from the city, at the Center for Research and Education in Science and Technology (CREST), which is another campus of the Indian Insititute of Astrophysics. We, however, decided to make a start and set up the apparatus at Bangalore so that the difficulties that may arise in the initial stages may be somewhat mitigated by the help that is available in a city, known to be one of the major technological centers of the country. Moreover CREST itself was under construction and the facilities there were still in their infancy. Accordingly

the laboratory space at IIA, Bangalore was partitioned into four cabins, two of which were designated as 'clean rooms'. These were equipped with a ducted air-conditioning system which pumped in filtered (20 μm) air. The rooms were maintained at a positive pressure to prevent dust from seeping into the room. While we could not measure the cleanliness that was obtained, we did follow the standard practices of a class 100,000 clean room and it made a considerable difference in the dust levels from outside to inside. The amplitude of the temperature variation during a typical day was about 2 deg. Centigrade. The chambers were supported on a table-frame which was built to our specifications and was very rigid. The legs of the table rested on four passive isolators from Newport (SLM 3A) and all cooling fans on the turbo-pumps were removed and mounted on separate posts. These had no mechanical contact with the table. The fore-pumps were connected to the turbo-pumps with light flexible PVC hoses. These steps reduced the chief sources of vibration in the apparatus. The vibrational frequency of the turbo molecular pumps being 833 Hz and 1.5 kHz, these did not couple very well to the rest of the system. The resulting level of vibration was sufficiently low as to allow us to observe the Fizeau fringes in the wedge without difficulty.

3.3 Preparation of the vacuum system

The assembly of the apparatus typically takes several months. The various sections of the vacuum system are cleaned according to standard vacuum practices. They are first washed with a weak soap solution (Teepol) and then rinsed with distilled water several times. They are then allowed to dry and wiped clean with lint-free tissue wetted with iso-propyl alcohol. The main interaction chamber had a matrix of blind tapped holes. These were cleaned with a high pressure jet of water mixed with soap solution. The screws used in such holes were vacuum relieved. The smaller parts were all cleaned in an ultrasonic cleaner in three stages (soap solution, distilled water and isopropyl alcohol). The parts were then carried into clean rooms and left to dry. They were typically given another wipe with fresh lint free tissue before assembly.

Any part that was exposed to vacuum environment was handled with care so as to not leave any finger print on it. Powder-free latex or plastic gloves were used to handle such parts. The tools used to assemble parts inside the vacuum chamber were also cleaned similarly.

After the vacuum chamber is assembled and the alignment of various parts of the chamber is completed it is closed and pumped down to the base pressure of the turbo-pumps. This process takes about a week and includes a three day bake at 150 deg.C. During this phase no gas is loaded into the reservoir however the source is allowed to discharge into the collimation chamber in order to remove the residual gasses as much as possible. The pressure in the various chambers stabilise at about 4×10^{-10} Torr (as measured with the gatevalve-1 shut-off) and then the reservoir is filled with the desired gas mixture as described below.

While filling the source one has to be cautious not to allow a large throughput into the collimation chamber since a sudden rise in pressure might damage either the hot cathode gauge or cause the turbo-pump to trip-off. In case the RGA is on, one makes sure that the gate-valve no.1 is half shut so that a sudden large flux of atoms does not reach the detector. When the On/Off valves on the gas lines are opened, the gas that has accumulated behind the valve is usually at high pressure and can cause an in-rush of gas if opened without caution. The rotary-vane pump on the source is therefore switched on prior to opening the valve on the gas line in order to absorb the initial pulse. The gas line and the source are pumped down using the rotary-vane pump. Up to this point the leak-valves are kept at minimum leak position. Once the pressure in the reservoir has reached its minimum (around 5×10^{-2} Torr) the rotary-vane pump is valved off. It is, however, kept in 'on' condition till the completion of the filling procedure so that it is available in case of any accidental in-rush while setting up the mixture. The pressure in the reservoir is held low by the loss of gas through the capillary array as long as the leak valves are all at minimum leak condition. The pressure in the collimation chamber is about 5×10^{-8} Torr when the source pressure is at its minimum. Then the He On/Off valve is carefully opened till the pressure in the collimation chamber reaches about 5×10^{-6} Torr. The beam count

rate at this pressure is about 500 counts per sec. Then the Xe leak-valve is opened till the pressure in the collimation chamber rises to 1.5×10^{-5} Torr. It was determined that the count-rate of Xe does not increase even if the partial pressure of Xe is increased beyond this amount due to a reduction of the mean free path below the chamber dimensions. This difficulty will be addressed in a future design of the source.

After completion of the procedure described above, it takes about a day for the count-rate of the various species to stabilise. While the actual observation of transmission of atoms through the cavity may take only a few hours the stability of the system is studied for several days in order to ensure that a steady state has been achieved with respect to all the atomic species under observation. Then the cavity is moved into place and the alignment procedure as explained in sec 2.5.2 is executed. After a desired spacing is positioned in the path of the beam, the transmission of several species is recorded as described in sec 3.9. We now describe the procedure adopted to measure the width of the gap between the plates.

3.4 Measurement of the width of the spacing between the surfaces

The assembly of the gold coated glass surfaces to form a wedge is done before they are inserted into the vacuum chamber. The wedge once assembled had to retain its shape over the course of the experiment which could be several months. During its assembly the wedge spacing between the plates is monitored by observing Fizeau fringes formed in the wedge under monochromatic light. The holding screws of the steel cell are adjusted till parallel Fizeau fringes were obtained in the wedge. The pressure applied by the screws had to be minimal as the glass surfaces would otherwise buckle and lose the surface planarity. At the same time the pressure had to be sufficiently high to allow us to pick up the cell and insert it in the vacuum chamber without disturbing the wedge that has been assembled. After the wedge was assembled under these constraints, it was inserted into its holders inside the interaction chamber and the fringes were once again examined to ensure that the wedge has not been disturbed.

The wedge had to then survive the process of obtaining vacuum and it was a matter of concern whether differential thermal expansions in the steel cell during the bake-out process would change the shape of the wedge. Therefore the wedge was examined once again before the actual measurement of transmission to ensure its integrity and the measurement of the width of the gap described below is from this last set of observations.

A 632 nm (red) He-Ne laser beam expanded using and was made incident on the wedge through the glass viewports in the interaction chamber. This beam passed through the wedge and cast an intereference pattern on a screen placed on the other side of the chamber. The interference pattern could also be seen with the naked eye when seen at an angle without looking directly into the laser beam. After the wedge was mounted in the optical translation stages the gap between the surfaces was monitored for several days. As described above, Fizeau fringes generated by diffuse monochromatic light (632 nm He-Ne laser) were used for this purpose. In addition, the green alignment laser, which now traces the path of the atomic beam, is also incident on the wedge. The zone of the wedge that is being traversed by the atomic beam is thus marked by a green laser spot. The fringe pattern and the green spot were photographed using a Nikon F90X camera at various vertical positions of the wedge. The position of the green laser spot was noted on each photograph with respect to the fringe pattern. Counting the fringes between the line of contact at the bottom and the position of the green laser spot gave us a measurement of the spacing between the surfaces at the position of the atomic beam. The fringe pattern was stable under translation of the wedge over a period of several days. Once the relation between spacing and vertical position of the cavity was obtained the red He-Ne laser was switched off and only the vertical position of the cavity was noted for determining the spacing. One of the many photographs taken is shown in Fig. 3.1. Fig. 3.2 gives the relation between vertical position and the spacing between the surfaces at the position of the atomic beam. A linear fit to the data in the Fig. 3.2 gives $y = 0.295x + 0.91$ where y is the spacing and x is the vertical position. To obtain a desired spacing the wedge was moved to the corresponding vertical position

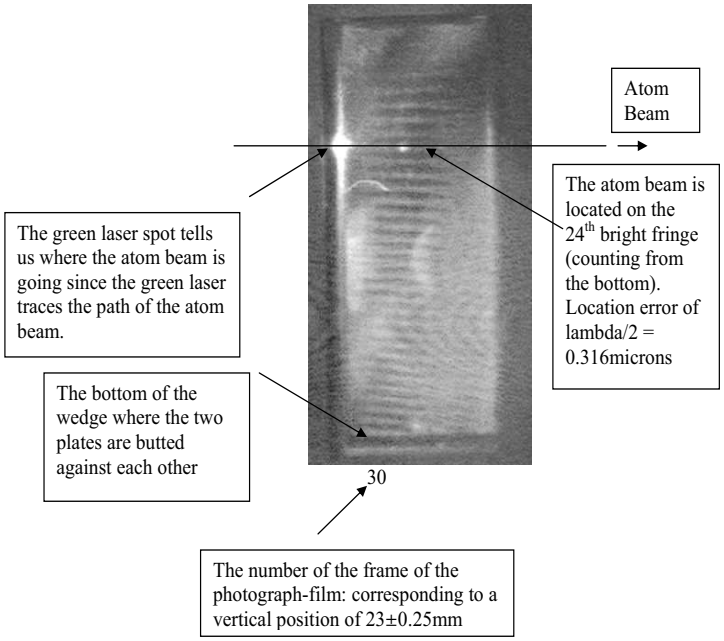

Fig. 3.1: A typical photograph of the fringe pattern which was used to determine the spacing between the surfaces.

as given by this relation.

3.5 Characterisation of the mass spectrometer

The mass spectrometer's structure and its basic functioning are described in 2.3. Here we present the various tests and optimisation runs we did to characterise it. This was done in three stages. The ioniser's parameters such as the electron energy and emission current had to be optimised for maximising the probability of ionisation for Xe atoms. Then we had to check the mass filter to establish the profile of the mass peaks for each of the species we were interested in. Lastly we had to determine the bias voltage at which we should operate the Continuous Dynode Electron Multiplier (CDEM) which would maximise its quantum efficiency while still providing a long working life for the unit.

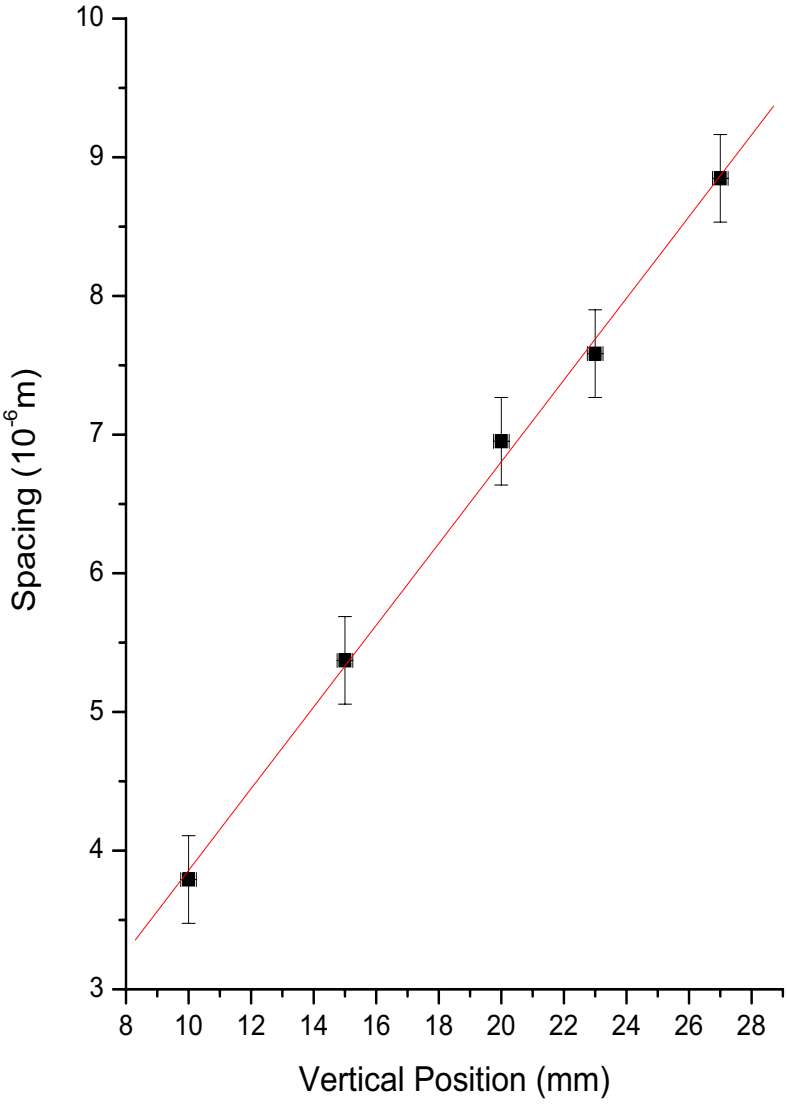

Fig. 3.2: The relation between the vertical position and the spacing between the surfaces at the atomic beam position is shown in this graph. The line shown on the graph is a linear fit to the data.

Atomic Species	Electron energy at maximum ionisation cross section (eV)	Maximum ionisation cross section (10^{-16} cm^2)	ionisation cross section at 105eV (10^{-16} cm^2)
He	145	38.1	37.3
Ar	105	298.4	298.4
Xe	125	590.6	581

Fig. 3.3: The ionisation probabilities of the He, Ar and Xe as reported in [15]. The cross sections are reported in units of $10^{-16} cm^2$

3.5.1 Optimisation of the ioniser parameters

The ioniser generates electrons by thermionic emission from a hot tungsten filament. These are accelerated to about 80 to 100 eV and confined into a cylindrical volume inside the ioniser by a reflection grid maintained at a potential lower than the -150V. An atom entering this volume under goes interaction with an energetic electron and is ionised. The probability cross section for this process is about 5×10^{-16}cm^2 for Xe. Though ionisation occurs over a range of electron energies starting from 20 eV to 1000 eV and beyond, the peak ionisation efficiency occurs at a specific energy for each atomic species. For Xe this occurs at 125 eV. However the maximum electron energy that could be set in the RGA is 105 eV and at this energy the ionisation probability is shown in Fig. 3.3. We scanned the electron energy and recorded the ion count rate this data is shown in the Fig. 3.4

The electron emission current was similarly increased to 2 mA to maximise the count rate. Increasing it beyond that did not increase the ion current. We interpret this as being due to the maximisation of the space charge density at this electron energy. The positively charged ions see a potential minimum along the axis of the space charge which being made up of electrons is negatively charged. The ions have to be extracted from this potential well by an extraction voltage and propelled in to the mass filter. This done by a focus plate which is maintained at -135 V. This

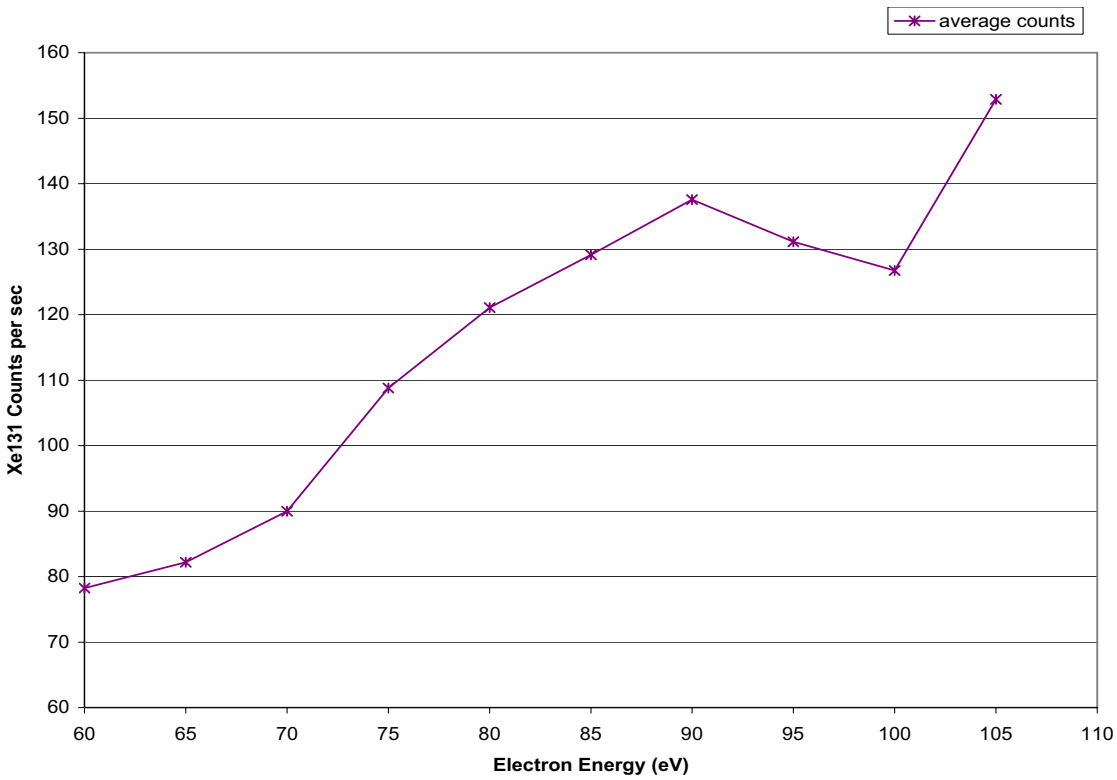

Fig. 3.4: The data showing counts as a function of electron energy for ^{132}Xe

attracts the ions from the space charge and at the same time reflects the energetic electrons thus preventing their entry into the mass-filter area.

The electronics of the RGA controls the frequency and amplitude of the AC and DC voltages that are applied on the quadrupole electrodes. These are factory calibrated and we checked the calibration of the mass scale by observing the counts as a function of the mass setting over the range of 128 to 140 amu. The results are shown in Fig. 3.5. This served two purposes. First it established that the mass scale is properly calibrated showing peaks at expected masses. Since Xe natural abundance is known the various isotopes could easily identified and their mass read off from the scale. Second it also established that the mass resolution of the RGA is better than 0.5 amu at 10% of the beam height. The profile of the peaks as can be seen are reasonably flat which decreases concerns of a shift the pass band of the filter changing with time due to small drifts resulting in loss of calibration.

3.5.2 The Continuous Dynode Electron Multiplier (CDEM)

The ions selected by the mass filter traversed its axis along stable trajectories and reached the back of the mass spectrometer where they were detected by a CDEM (Model 2120 from Detech). This was factory installed and was not handled by us in any way. However several characterisation runs to determine the optimal bias voltage and pulse height discrimination voltage were performed. These results are presented below. The CDEM generates an electron cascade in response to an ion arriving at its entrance. The cascade produces about 10^8 electrons at about 2000 V of bias across the CDEM. The average number of electrons produced per ion is known as the gain of the CDEM and is a linear function of the bais voltage. However the gain of the CDEM changes over its lifetime, which is about 10^{11} counts and it also changes if it is exposed to any contamination. While contamination was not a concern in this vacuum system since there were no corrosive gasses or hydrocarbon deposits, ageing of the CDEM was a major concern. Therefore the flux of ions incident on the CDEM was always controlled cautiously in the experiment. The gain of the CDEM was observed as a function of the bias voltage and the data is shown in the Fig. 3.6. The electrons produced by the CDEM, are collected by an anode plate and shunted through a 50 ohm resistor to ground. The resulting negative pulse of $\approx 10^{-9}$s in width and ≈ -25mV in height can be counted by the SR400 photon counter. However these ion detection pulses have to be distinguished from the background electromagnetic noise. In order to do this the CDEM bias voltage has be to high enough to produce a detection pulse that is at least a factor of two taller than the noise pulses. The counts as a function of the pulse height were observed in order to decide an optimal discriminator threshold. The data is plotted in Fig. 3.7. The discriminator voltage scan was repeated with the filament in the ioniser switched off so that ion flux was eliminated and only electromagnetic noise may be observed. It is to be noted that there were no noise pulses beyond -4 mV. Based on this information a discriminator voltage of -6 mV was selected for counting ions arriving at the detector.

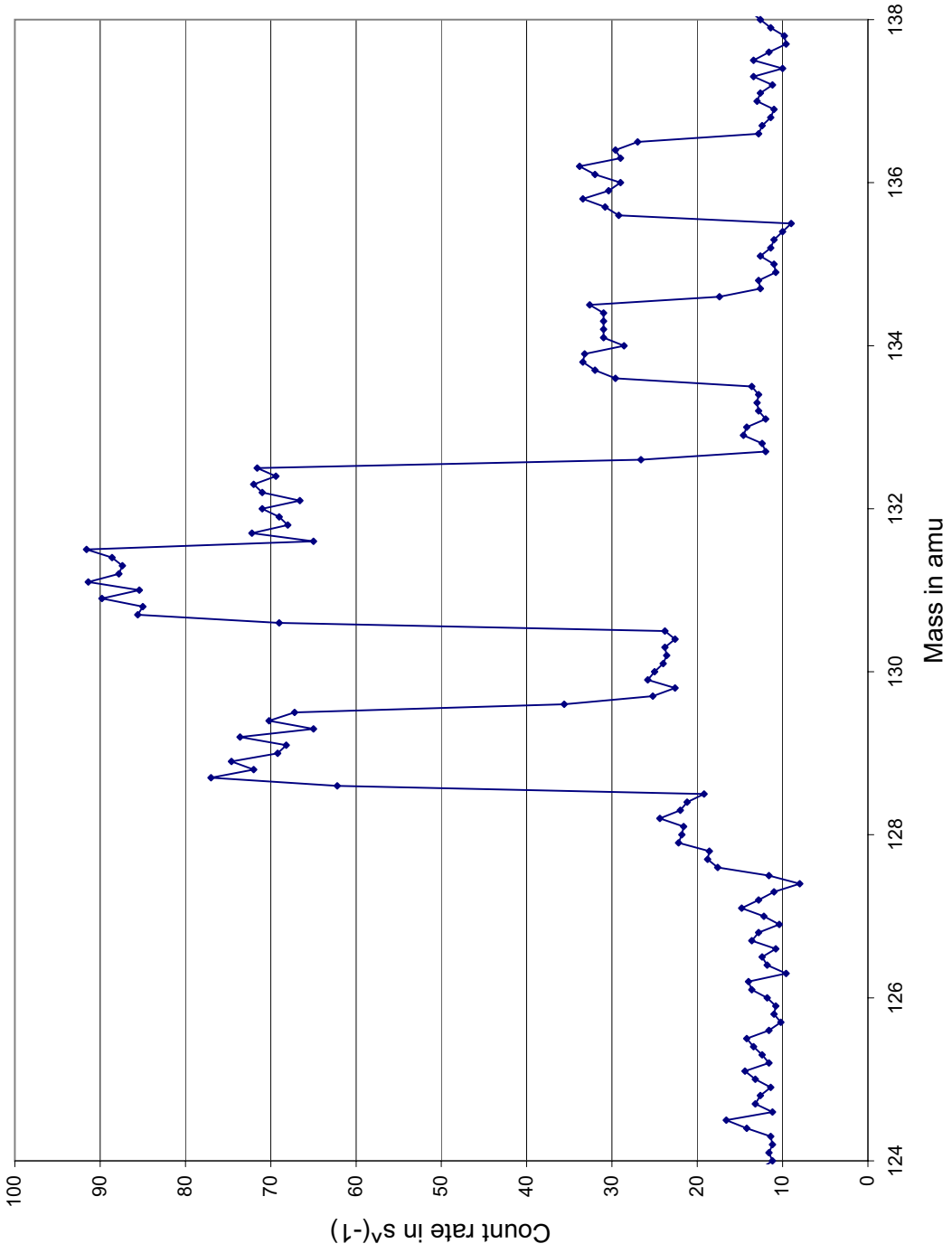

Fig. 3.5: Counts as a function of mass showing mass-scale calibration, mass resolution and profile of the mass-peaks.

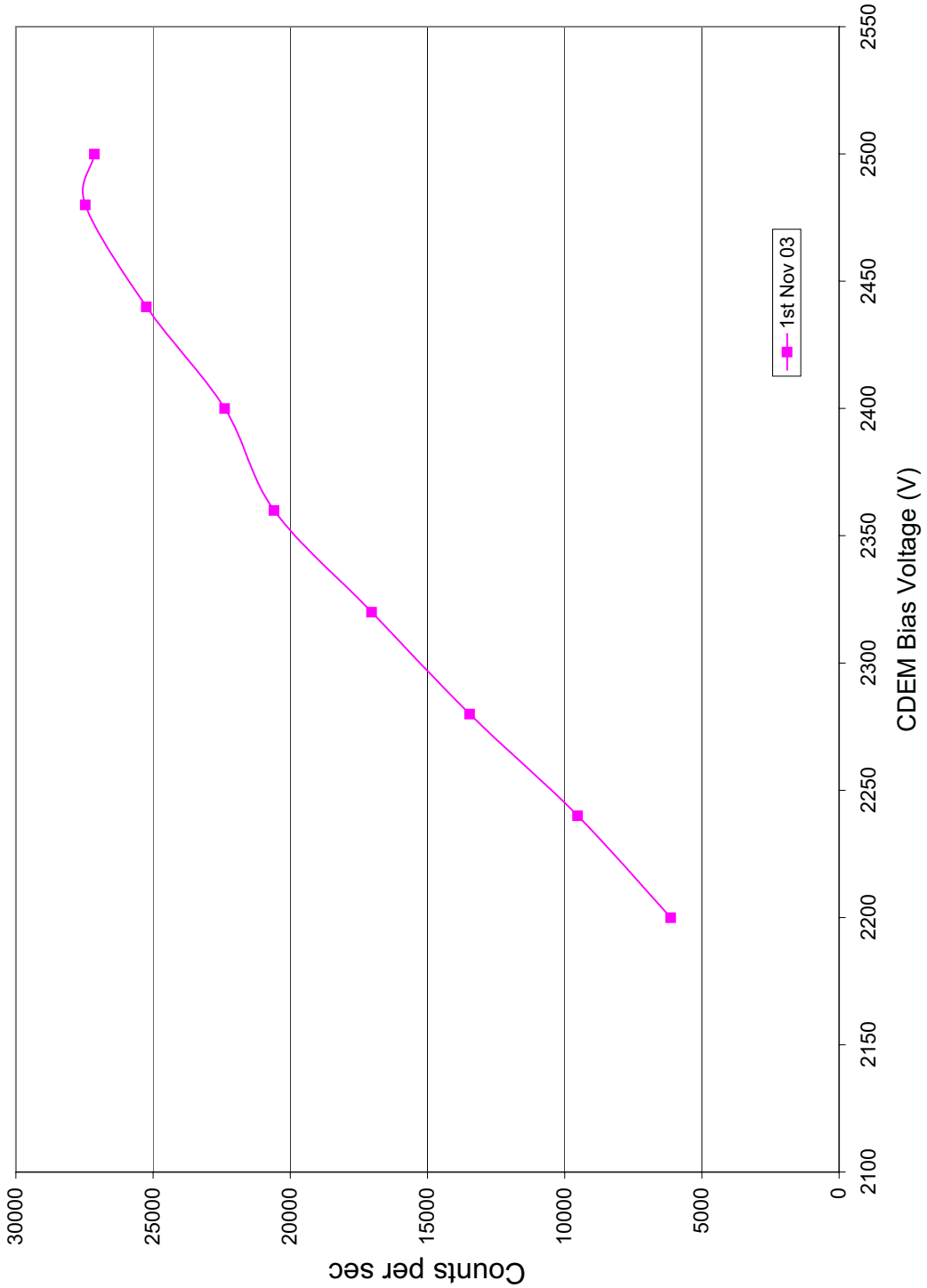

Fig. 3.6: Counts as a function of CDEM bias voltage showing the gain of the CDEM as a function of bias voltage.

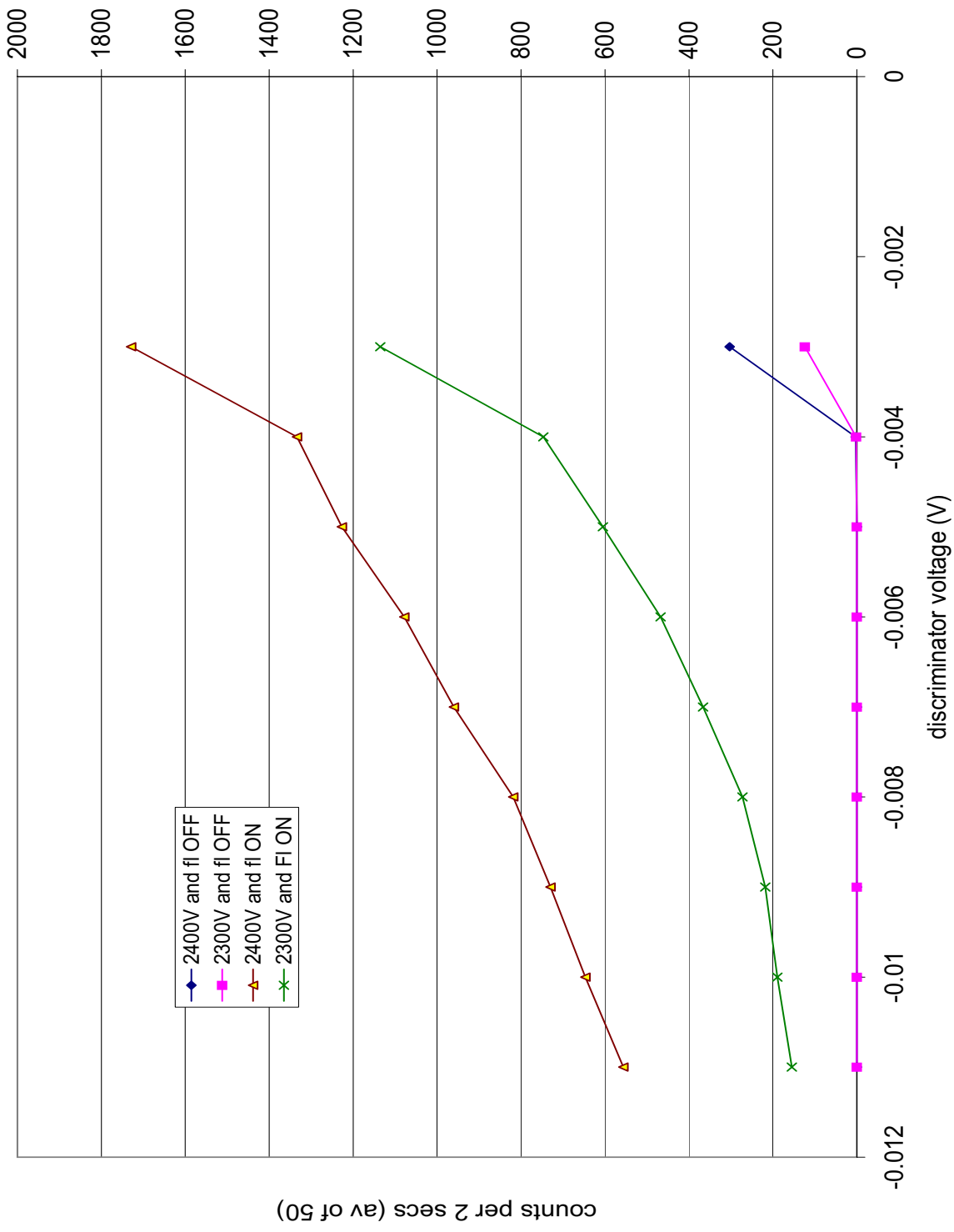

Fig. 3.7: Counts as a function of discriminator voltage on the counter showing the sharp decrease of noise at -4mV.

3.6 Actuator calibration

The positioning of the wedge in the beam is achieved by moving the various translation and rotation stages by using the actuators on them. The picomotor actuators (from Newfocus Inc.) had a mean step size of about 30 nm but did not generate any feed back on the amount of movement that the tip of the actuator underwent for one pulse from controller. The step size of the actuator was also not a constant and was known to change with load and ageing. Since it was dependant upon friction within the actuator the actual step was not predictable. As a result of these factors the actuators had to be calibrated in-situ under the actual load and UHV conditions. At the end of this process the ability to retrace a movement reliably was established. The rotation axis of the optical mount did not coincide with the edge of the cavity where the atom beam was incident. If the axis does not coincide with the entry side of the cavity it would not be possible to decouple the translations from rotations. However using horizontal translation stage the effective rotation axis could be shifted to the desired location by undoing the unwanted translations. These calibrations took considerable time and effort before we could develop a reliable technique to obtain predictable movements of the cavity. The differences and asymmetries were accommodated by compensating for them in the control software and in the end were invisible to the experimenter.

3.7 Gold Coatings

The gold coatings were done by Hind High Vacuum Co. Ltd at Bangalore. The cleaned glass plates were loaded onto a turntable in a vacuum chamber and an initial vacuum of about 10^{-6} Torr was obtained with a diffusion pump. The temperature of the substrate was raised by radiation from a hot tungsten heater to about 200 deg.C. Gold placed in a molybdenum 'boat' was evaporated by resistive heating of the boat and the vapour was deposited on the substrates. During the coating the pressure in the chamber was about 10^{-4} Torr. The coating thickness was monitored by a crystal oscillator. The thickness required was calibrated ahead of time, by a few sample runs

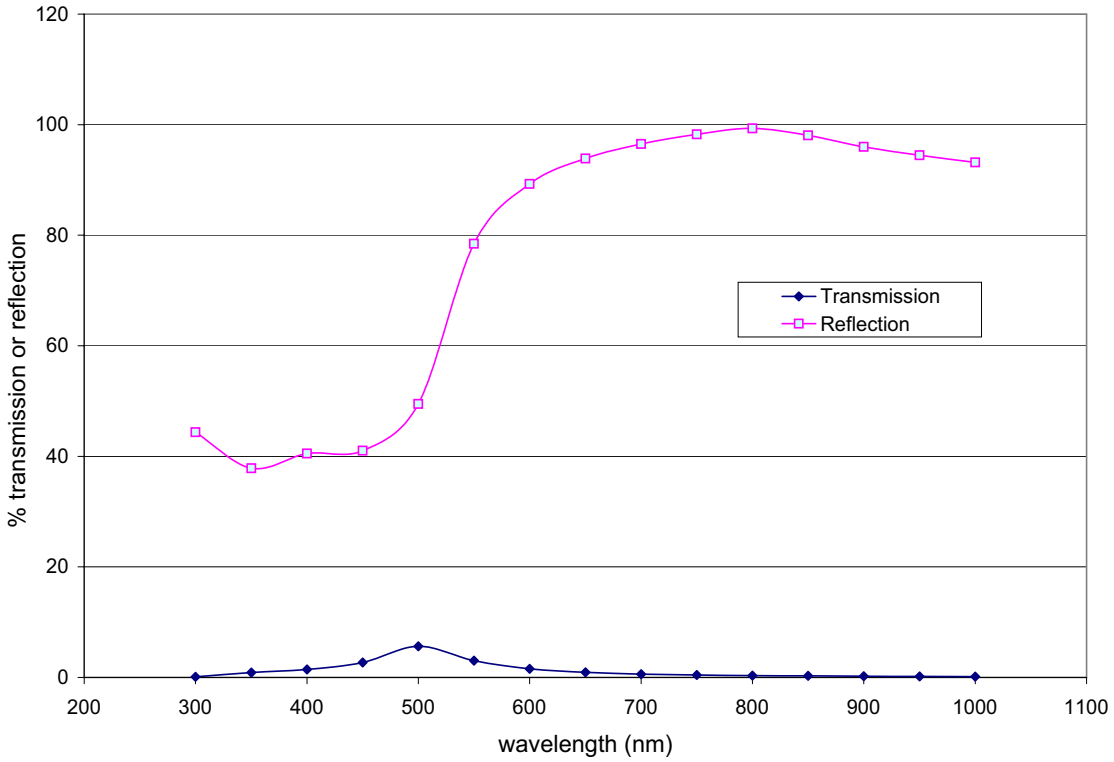

Fig. 3.8: The transmission and percentage reflectivity of the gold layer.

onto float-glass substrates to determine the appropriate thickness for obtaining a 1% optical transmission at 600 nm. A layer of 400 Å was deposited at the rate of 5 to 8 Å for the final coating done. This was done in two stages so that the dust particles on the surface could be brushed away and would not leave pin-holes of uncoated area. The transmission of the gold layer as a fraction of the incident light was measured and is plotted in Fig. 3.8. The same figure also reports the reflectivity of the gold layer normalised to that of a freshly coated aluminium. This data is tabulated in Fig. 3.9.

3.8 Transmission through the system without the cavity plates

The stability of the incident beam was observed several times during the course of the experiment. These data reflect the composition of the beam incident on the cavity. The isotopic composition of Xe in the source reservoir is expected to be close to the average natural abundance. However the flux of Xe isotopes is proportional to the

Wavelength(nm]	T(%)	R(%)
300	0.1	44.37
350	0.89	37.83
400	1.45	40.5
450	2.7	41.03
500	5.64	49.46
550	3.05	78.44
600	1.55	89.28
650	0.93	93.88
700	0.61	96.51
750	0.44	98.25
800	0.34	99.32
850	0.28	98.05
900	0.22	95.98
950	0.2	94.48
1000	0.16	93.16

Fig. 3.9: The data on the transmission and reflection co-efficients of the gold layer.

velocity of the atoms and consequently to $\frac{1}{\sqrt{m}}$, where m is the atomic mass. One set of the observations of the direct beam is shown in Fig. 3.10

Some of the typical steps involved in the initial stages of the experiment are also apparent in this figure. The adjustment of the He partial pressure in the source so as to obtain an optimal flux of He without suppressing the Xe flux is shown. The gradual stabilisation of He flux over the course of an hour is also visible between 1900 and 1950 mins. Such direct beam observations were repeated on several days till we obtained an optimal beam composition with a stable beam intensity.

3.9 Observation of transmission through the cavity

After observations of the direct beam we proceeded to position the cavity in the beam and record the ion flux received at the RGA. These two stages of the experiment are (position and record) are repeated at each chosen spacing. A complete measurement at one spacing is considered one run of the experiment and takes about 24hrs. The observed flux at a spacing of ten microns is about 5% of the direct beam flux. A large portion of the observed flux is of course due to the diffuse background.

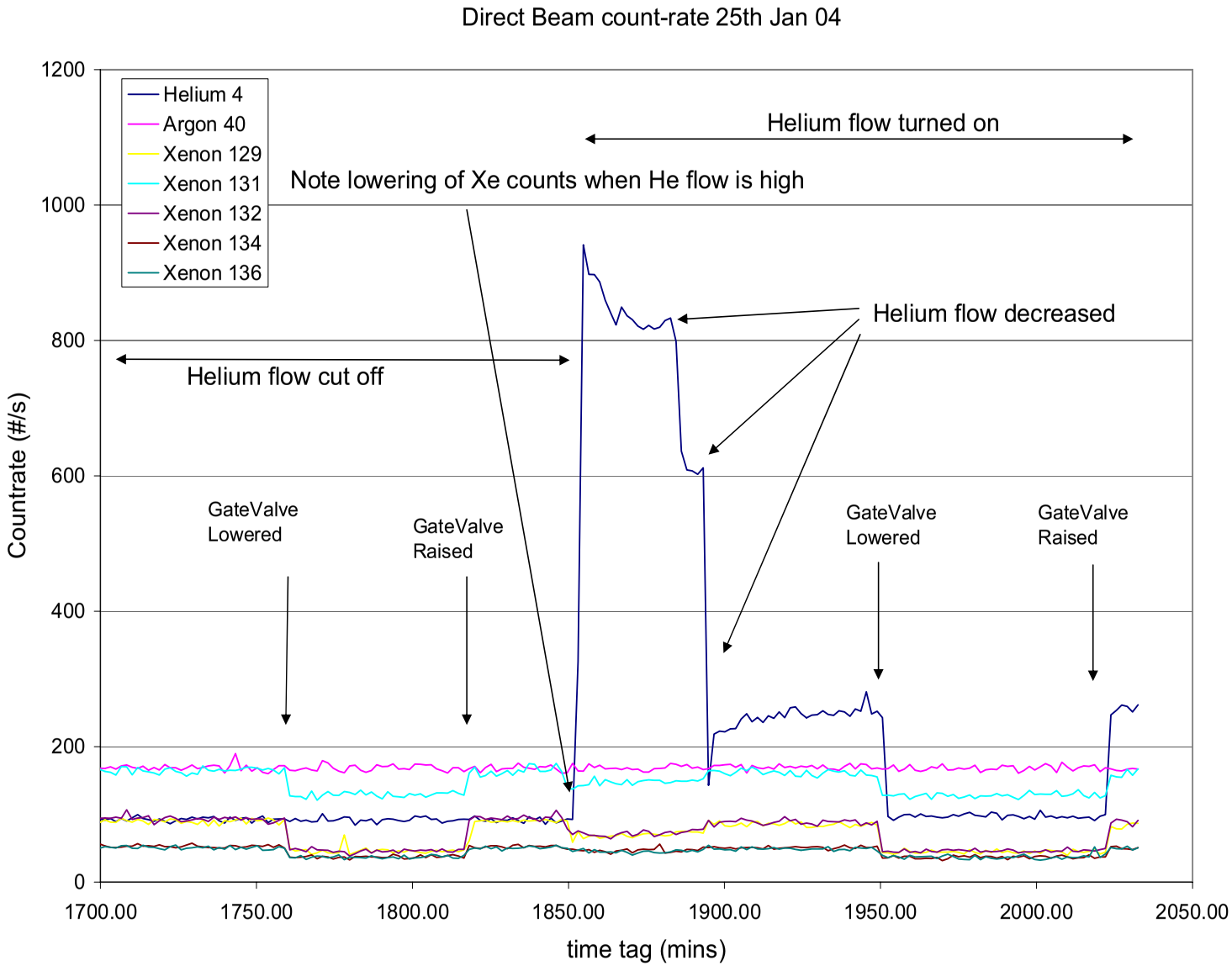

Fig. 3.10: The flux of atoms at various masses in the incident beam as a function of time. The blocking of the beam by a half closed gate valve allows us to measure the background. The background and beam fluxes were thus measured alternately by operating the gate valve.

3.9.1 A typical run: Stage 1

Once the cavity is located in the beam and made parallel to it (good to about 200 milli radians) we translate it upwards and position the desired cavity width at the beam location. Then a slow rotation scan of the cavity is performed in small angular steps(2 mrad to 10 mrad steps). Between every two steps we measure the average He flux. We position the cavity at the location of maximum He flux. The movements of the cavity and recording of the He flux is performed through the PC interfaced to various instruments. This alignment may take up to 8 hrs or longer since the mechanical system takes time to relax and the low flux levels at smaller cavity widths force us to integrate for longer time at each angular position during the scan.

3.9.2 A typical run: Stage 2

After optimal alignment was reached the transmission of various species of atoms was recorded at that spacing. The flux of each species was measured for a short duration of time lasting approximately a few tens of seconds. The duration of observation for a particular species was chosen to be in proportion to the reciprocal of its flux above background. A set of seven species ($He, Ar, ^{129}Xe, ^{131}Xe, ^{132}Xe, ^{134}Xe, ^{136}Xe$) were each observed one after another in a sequence. The duration of one such sequence was about 480 secs. Then the whole sequence was repeated again in the same order. In this fashion the flux was observed for several hours till the total number of counts(above background) observed at each species was larger than 10,000. The duration of observation of each species is tabulated in Fig. 3.11.

The flux (counts per sec) thus observed as a function of time is shown in the following figures for three spacings, 12.7 μm, 10 μm and 8 μm. Observations from one of these measurements are shown in Fig. 3.12 to illustrate a typical raw-data set.

In order to obtain a measure of the flux arising from the background gas density we blocked the beam in front of the source by half closing a gate valve (no.1 in Fig. 2.6). The effect of cutting off the beam is most clearly visible in the He flux which shows several clear steps. The highs correspond to the beam 'ON' condition and the lows

Atom	Mass(amu)	time (s)
He	4	10
Ar	40	50
Xe	129	50
Xe	131	50
Xe	132	50
Xe	134	100
Xe	136	100

Fig. 3.11: The duration of observation of flux at each atomic mass. This duration was selected so that we obtain roughly equal number of atoms at each mass over the duration of the experiment.

to beam 'OFF'.

Once the ON and OFF conditions are observed for several hours at one cavity spacing we reposition the cavity at a different spacing and repeat the measurement process.

We would like to attention to several features of the data.

Argon was not loaded into the reservoir and hence was not a beam component. It is, however, present in the background as we had earlier used Argon during the early stages of the experiment. Note that closing and opening the gate valve has little or no effect on the argon flux.

The data shows fluctuations over short time durations that are much larger than the expected level of statistical fluctuations. For example in Fig. 3.12 consider He at a flux level of 125 counts per sec. Note that the flux is averaged over 10 s and hence expected statistical error on this observation is about 3.5 counts per sec. Yet within a few hundred seconds we observe fluctuations larger than 10 counts per sec. Such short duration fluctuations could not arise in the background gas density or the incident beam intensity as both these quantities are governed by static, passive components such as slits, leak valves and the capillary array. These fluctuations were later traced to fluctuations in the gain of the RGA.

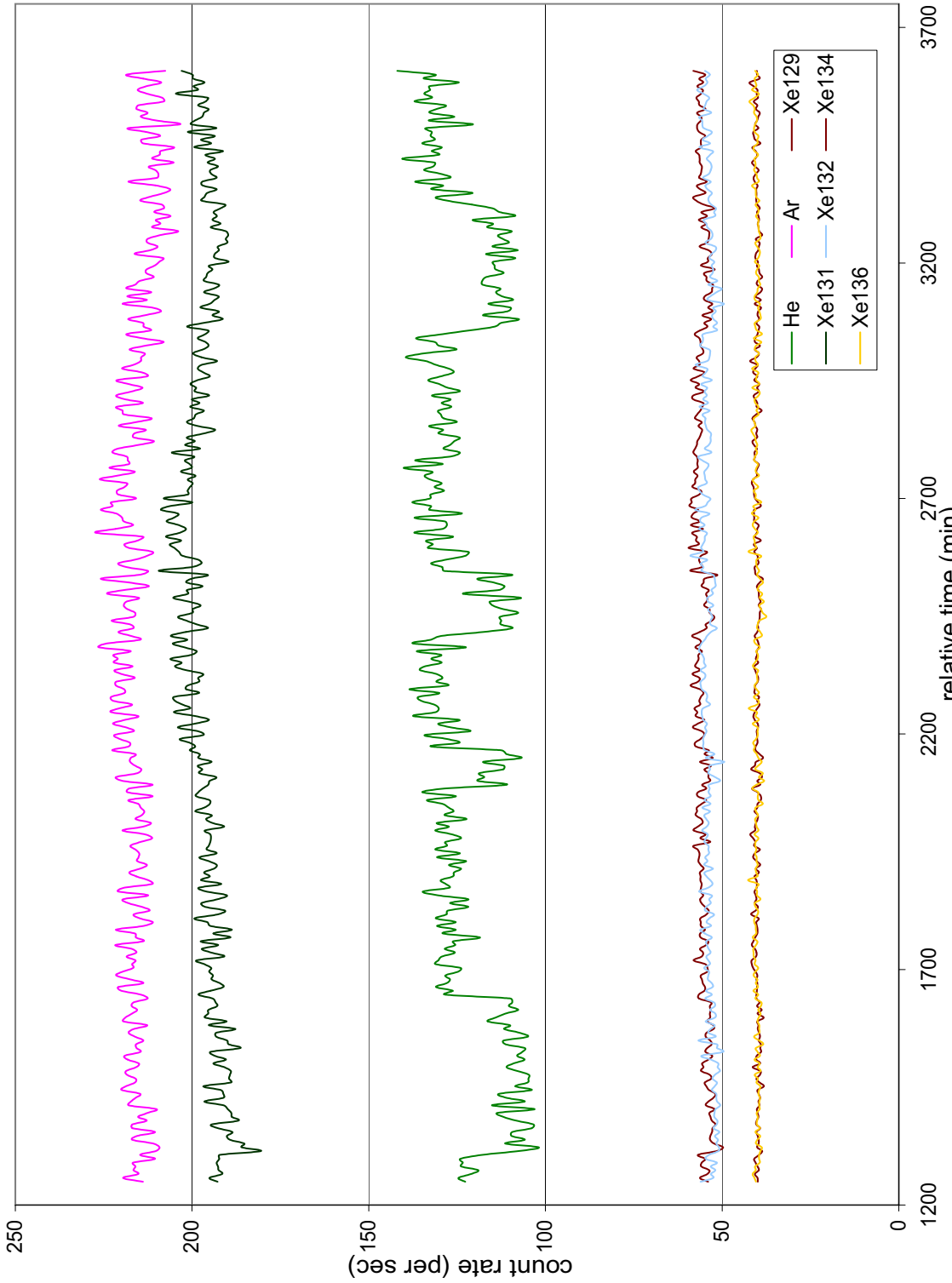

Fig. 3.12: The transmitted flux at various masses through a cavity of width = 10 μm

There also drifts in the flux over longer durations of several hours which made it difficult to compare observations of one spacing with another since these two sets of observations were typically one to two days apart. We attempted to estimate these variations over time and correct for them. We describe three such attempts in the next chapter.

4. ANALYSIS AND RESULTS

Abstract

The observed flux from the direct beam and the flux transmitted through the cavity both had large fluctuations and drifts. To correct for these drifts two correction methods were attempted to estimate the variations in the efficiency of the detector and the background partial pressures. However these methods could not correct for drifts of all the species. We therefore chose to examine the total flux of each Xe isotope relative that of ^{132}Xe. When this quantity was tabulated under various experimental conditions, a consistent pattern emerged.

4.1 Introduction

In order to deduce a relation between the cavity spacing and the atomic flux through the cavity, it was necessary that the data be corrected for drifts over the long duration over which it was collected. These drifts could arise from a combination of variations in the incident beam intensity, detector efficiency and background gas density.

Variations in the detector efficiency could arise due to drifts at any of the three stages of the RGA (ioniser, mass filter or the CDEM detector). Flux observed at a constant mass setting does not show variations beyond those expected from the counting statistics. Nor does a mass-scan, where the pass band of the mass filter is incremented in small steps, show these large fluctuations. Therefore there is, at this point, no evidence indicating instability in the RGA.

The background gas in the detection chamber comprises of species arising from out-gassing as well as those present in the atomic beam. However, we are not sensitive to species other than the ones selected for observation, of which only Ar is present

in any appreciable quantity in the atmosphere. Therefore the background density of all the species (other than Ar) arises solely from the atomic beam itself. Hence in the rest of the document 'background gas' refers only to the species of interest and does not include the other species typically present in a UHV chamber. The gas density in the collimation chamber is high and the gas diffuses into the interaction chamber and from there into the detection chamber. This diffusion is one source which adds to the partial pressure of the background gas in the detection chamber. The other source is the scattered beam from the sides of the cavity which then finds its way into the detection chamber. However the contribution of this is expected to be a small fraction of the total throughput into the interaction chamber. The former component was measured in the beam OFF condition (half closed position of gatevalve-1 in Fig. 2.3) and subtracted from the flux received in the beam ON condition. To estimate the latter the cavity would have to be translated or rotated till the direct beam flux is cut off. To realign the cavity to the beam would then typically take a day or more. Therefore this quantity could not be measured during the course of the experiment.

The mass spectrometer (RGA) is not sensitive to the direction from which the flux of atoms arrive, therefore it does not distinguish between directed atomic beams and the undirected background gas. While the solid angle from which the background gas arrives is the entire forward hemisphere (2π st.rad), the beam arrives in an extremely narrow solid angle ($\approx 10^{-7}$ st.rad). Also while the background flux is present over the entire surface area of the ioniser (≈ 10 cm^2) the beam cross section is very small ($\approx 10^{-2}$ cm^2). Due to this large area-solid-angle-product ratio ($2\pi \times 10^{10}$), variations in the background partial pressure (of the atomic species under consideration) are the chief source of drifts in the experiment.

Our attempts to model these drifts and correct for them is described in the following two sections.

4.2 The Corrections for drifts

We start with the assumption that the direct beam intensity does not change with time over the duration of the observation. We shall attribute all changes of the observed flux (O) to changes in efficiency (ϵ) of the detector and the flux (b) from the background . The flux transmitted through the cavity (s), which constitutes the 'signal', is assumed to be constant.

Consider the flux of any one species. The observed flux in the beam ON condition, $On(t)$, of that species is given by,

$$On(t) = \epsilon(t)\,[s + b(t)] \tag{4.1}$$

and that in the beam off condition $Off(t)$ is given by,

$$Off(t) = \epsilon(t) \cdot b(t) \tag{4.2}$$

If one obtains an estimate of $\epsilon(t)$ then the data can be corrected by this factor and then $b(t)$ may be subtracted to obtain s. This is the route chosen in Method 1.

On the other other hand by obtaining a fit to the data in the beam OFF condition the functional form of $\epsilon(t) \cdot b(t)$ can be obtained. This can then be subtracted from $On(t)$ and the resulting data ($\epsilon(t) \cdot s$) can then be corrected for ϵ. This is the route explored in Method 2.

4.2.1 Method 1

The data shows correlations between the fluxes of He, Ar and ^{131}Xe (refer Fig. 4.1). Since Ar is not a beamed species one does not expect its intensity to be correlated to a species in the beam. Therefore these correlations could only arise due to changes in detector efficiency over time. If one assumes the Ar density to be constant over several hours, then, changes in the observed Ar flux can be attributed to changes in the efficiency of the detector. We can therefore define changes in the detector efficiency as a relative deviation of Ar flux from its mean value over a single run of the experiment. Efficiency thus obtained was used to correct the fluxes of all other

species by dividing them by this efficiency factor.

The data after efficiency correction and background subtraction is tabulated in the following Fig. 4.2. The same data is plotted in Fig. 4.3. Since He is not significantly affected by the Casimir-Polder force we expect the He flux to show a quadratic dependance on the cavity spacing as required by a simple geometric effect. However such a dependance is not seen in the data.

There are several possible reasons for the failure of this method. The assumption of the constancy of Ar background could be wrong. On the other hand estimation of $\epsilon(t)$ from the beam ON data is unreliable since the changes due to the background $b(t)$ will also be present simultaneously. We then examined the possibility that temperature variations could be the cause of the variations in flux. However temperature variations affect all the species by the same factor $\sqrt{T}$ and would have been corrected in the above method.

During the observation of flux through a certain cavity width, a large fraction of the observed flux is from the diffuse background gas in the detection chamber. Since most of the gas scattered off the cavity walls will contribute to the background gas density, it prompted us to explore *Method 2* .

4.2.2 Method 2

It is not possible to individually evaluate either $\epsilon(t)$ or $b(t)$ in a single step. However we can obtain knowledge of the product $\epsilon(t) \cdot s$ by first obtaining a linear(or low order polynomial) fit to the $Off(t)$ for each species. By subtracting this from the $On(t)$ of the corresponding species it would be possible to isolate the $\epsilon(t) \cdot s$. If there is an efficiency change common to all the species it would show up at this stage as a strong correlation among all species in these residues.

It was also realised that ^{131}Xe contained a large flux from an atmospheric fluorocarbons at the same mass. Evidence of this can be seen, for example in Fig. 3.4, where ^{131}Xe vs electron energy shows a minor peak at 90 eV, a feature not seen in the data of [15]. This anomaly also shows up in the mass spectrum shown in Fig. 3.5 where the

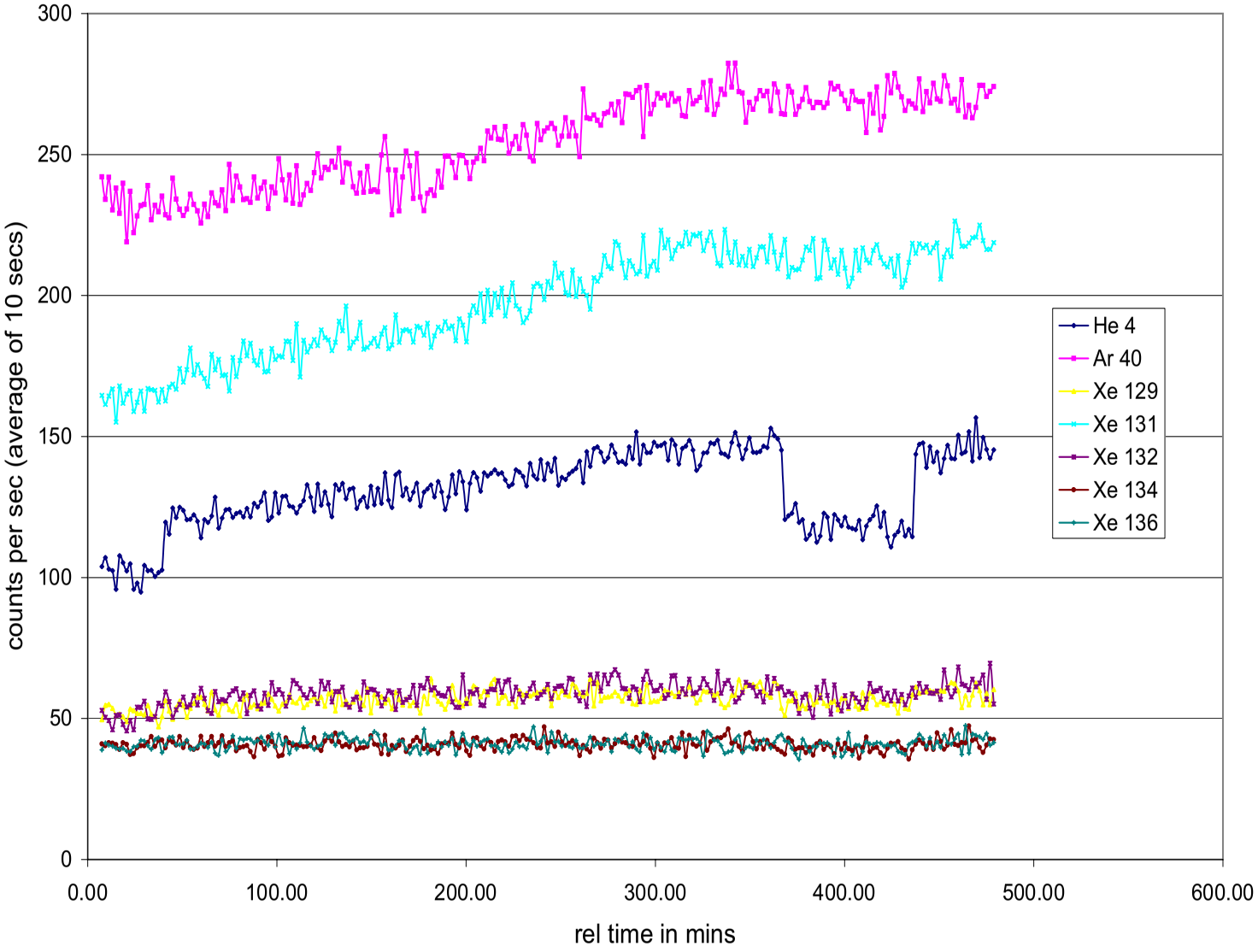

Fig. 4.1: The transmitted flux at various masses through a cavity of width = 12.7 μm. Note the correlated variations of He, Ar and ^{131}Xe. These indicate a possible variation in efficiency of the detector.

	Average flux above background (counts per sec)						
spacing (μm)	He 4	Ar 40	Xe129	Xe131	Xe132	Xe134	Xe136
8	16.78	0.18	1.92	1.50	2.05	0.50	0.80
10	16.77	0.67	2.13	2.40	1.78	0.58	0.65
12.7	23.70	2.00	3.64	4.32	5.74	0.94	0.98

Fig. 4.2: The transmitted flux at various cavity spacings after correcting for fluctuations in efficiency and background flux. It was not possible to deduce a relationship between flux and cavity spacing even after applying the corrections.

$\frac{^{131}Xe}{^{132}Xe}$ ratio (=1.26) deviates from that normally found in air(0.79). Therefore the data on ^{131}Xe was not analyzed further. Similarly the data on Ar, which was not a beamed species was also dropped. The remaining data for beam on and off conditions was analyzed in an attempt to obtain a relation between flux and cavity width. Besides looking at the flux of individual Xe isotopes, we also looked at total Xe flux, as well as the ratios (a) $\frac{flux[i]}{flux[Xe132]}$ and (b)$\frac{flux[i]}{flux[Xe136]}$. These analyses are tabulated in 4.4.

These observations did not fit any simple model. The sampling of the $Off(t)$ function was insufficient to result in an accurate estimation of $\epsilon(t) \cdot b(t)$.

We, therefore, decided to look at isotope ratios of the *incident beam*. These at oms have passed through the 10 μm diameter capillaries in the capillary array of the source. We wished to examine if there is any deviation from the natural abundances (the sample of Xe available with us being obtained by air fractionation) in this data as compared to that of the background.

4.2.3 Method 3

We considered the portion of the data in which the direct beam flux was measured during the stability studies and added together all the flux obtained at each atomic mass. This gave us the *total number of atoms* observed at each mass in the direct beam. The measured flux in the beam ON condition includes both the atoms that have not suffered any deflection in their flight from the source, as well as those that

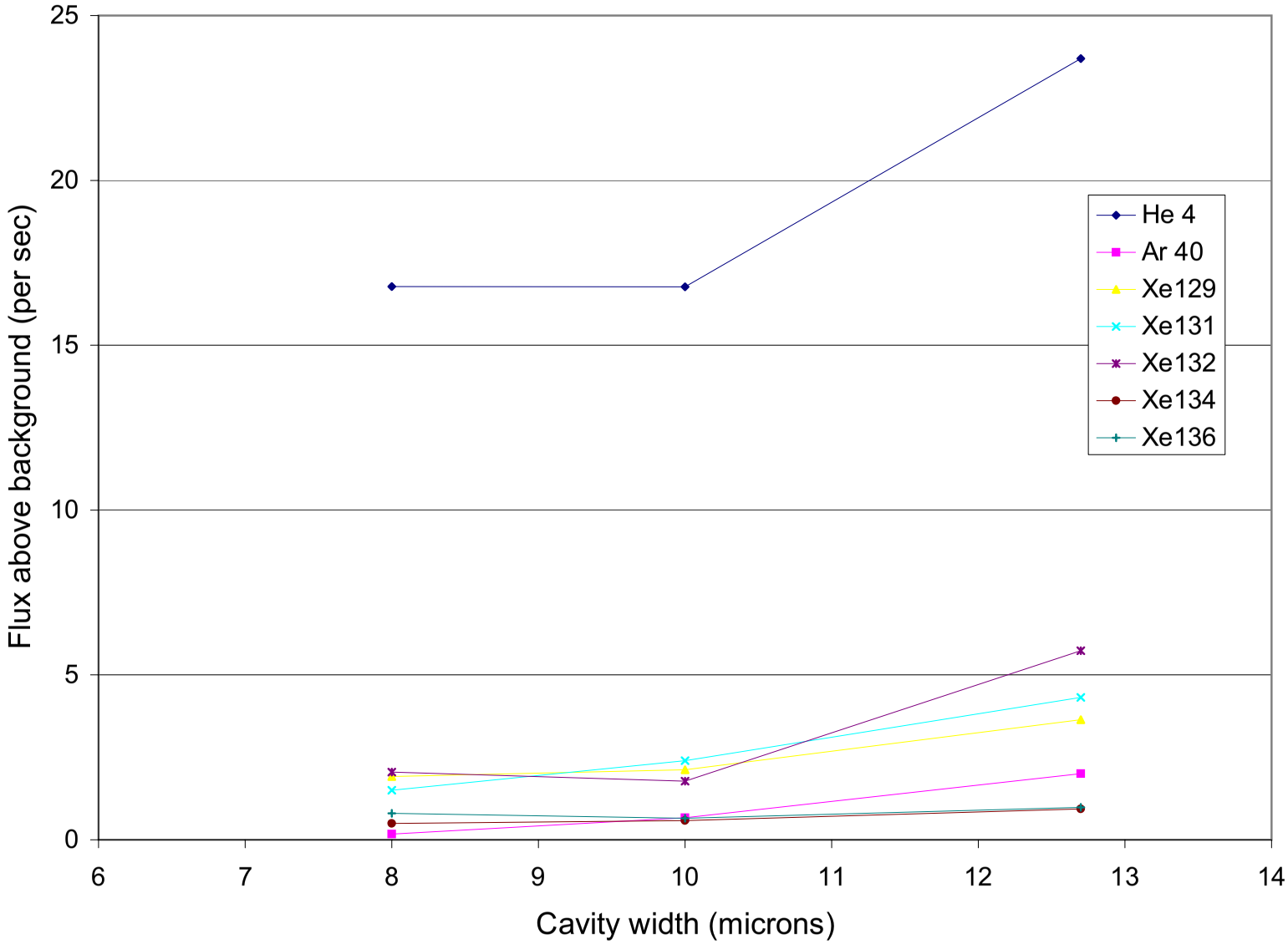

Fig. 4.3: A plot of the data shown in Fig. 4.2: The transmitted flux at various cavity spacings after correcting for fluctuations in efficiency and background flux.

Analysis 2	Difference in Flux(ON-OFF) (counts per sec)					
spacing (microns)	He	Xe129	Xe132	Xe134	Xe136	XeTotal
8	12.86	1.23	1.43	0.77	0.62	4.04
10	15.33	2.06	1.58	0.63	0.78	5.04
12.7	29.49	4.40	6.33	1.37	1.61	13.71
Analysis 2	Ratio(Xe[ ]/Xe[136])					
spacing (microns)	He	Xe129	Xe132	Xe134	Xe136	
8		1.99	2.32	1.26	1.00	
10		2.64	2.03	0.80	1.00	
12.7		2.73	3.92	0.85	1.00	
Analysis 2	Ratio(Xe[ ]/Xe[132])					
spacing (microns)	He	Xe129	Xe132	Xe134	Xe136	
8		0.85744	1	0.54219	0.43081	
10		1.3044	1	0.39732	0.49372	
12.7		0.6961	1	0.21688	0.25482	

Fig. 4.4: The transmitted flux at various cavity spacings after subtracting a fit to the background. The ratio of the fluxes to flux at ^{132}Xe and ^{136}Xe are also shown.

have been scattered. The observations taken in the beam OFF, $Off(t)$, condition would not contain the former unscattered component.

We also took all the observations of the beam OFF, $Off(t)$, condition in each run of the experiment, and summed the flux at each atomic mass. Next, the data set from each run was normalised to the total number of ^{132}Xe counts observed in that run. The result of these operations is shown in Fig. 4.5.

Two conclusions may be drawn from this table:
(a) the ratios are constant over the entire course of the experiment lasting over several weeks and
(b) the background flux is different from the beam ON to the beam OFF condition, which implies we cannot estimate the background from the beam OFF condition and subtract it from the ON condition.

Recall that to measure $Off(t)$, we close the gatevalve (no.1) to cut off the direct beam from reaching the detector. While the net throughput of the beam is very small (1%) compared to the flux in the background, the net inflow into the detection chamber would therefore be altered by a small amount by cutting off the beam.

We therefore wished to estimate the background present in each data set, we start with the assumption that a constant 'flux' arising from instrumental noise and the background gas density was added to all the species. Evidence of this may be seen in Fig. 3.5 where the constant instrumental background is seen. This constant background was estimated by further assuming that within a given set of data the ratio $\frac{^{136}Xe}{^{132}Xe}$ is the same as the natural ratio of 0.33. This estimated number was subtracted from each data set to obtain the true Xe flux that was observed at each mass. The ratio $\frac{^{m}Xe}{^{132}Xe}$ of this corrected flux, was then tabulated for each data set. These data are tabulated in 4.6. A comparison between Fig. 4.5 and Fig. 4.6 shows that the ratio $\frac{^{129}Xe}{^{132}Xe}$ is no longer constant in Fig. 4.6 across the various sets of data indicating that the process of subtracting a background has introduced errors into the data.

We are therefore limited by our lack of proper knowledge of the background flux at

Ratios of total counts received (#[Xe...]/#[Xe132])												
ON	through cavities			direct beam				average ratio				
spacing (μm) or date	12.7	10	8	7th Feb	27th Jan	25th Jan	31st Jan	thro cavity	error %	direct	error %	natural
Xe129	0.97	1.03	1.01	0.98	0.94	0.95	0.94	1.00	1.1	0.95	0.9	0.98
Xe132	1.00	1.00	1.00	1.00	1.00	1.00	1.00	1.00	7.4	1.00	0.0	1.00
Xe134	0.69	0.74	0.77	0.51	0.56	0.58	0.56	0.68	1.7	0.55	1.3	0.39
Xe136	0.70	0.74	0.77	0.52	0.54	0.56	0.54	0.68	1.8	0.54	0.9	0.33
OFF	through cavities			direct beam				average ratio				
spacing (μm) or date	12.7	10	8	7th Feb	27th Jan	25th Jan	31st Jan	thro cavity	error %	direct	error %	natural
Xe129	0.99	1.03	1.02	0.97	0.96	0.96	0.94	1.00	1.3	0.96	0.6	0.98
Xe132	1.00	1.00	1.00	1.00	1.00	1.00	1.00	1.00	0.0	1.00	0.0	1.00
Xe134	0.72	0.76	0.77	0.72	0.80	0.79	0.71	0.74	1.3	0.76	1.9	0.39
Xe136	0.73	0.76	0.78	0.73	0.80	0.79	0.70	0.75	1.1	0.75	2.1	0.33

Fig. 4.5: The transmitted flux at various cavity spacings and in the direct beam normalised to flux at ^{132}Xe. Note that the ratios in the direct beam are stable but different from that of any other data.

Ratios of total counts received (#[Xe...]/#[Xe132])												
ON	through cavities			direct beam				average ratio				
spacing (μm) or date	12.7	10	8	7thFeb	27th Jan	25th Jan	31st Jan	thro cavity	error %	direct	error %	natural
Xe129	0.93	1.10	1.04	0.99	0.93	0.93	0.92	1.02	2.8	0.94	1.4	0.98
Xe132	1.00	1.00	1.00	1.00	1.00	1.00	1.00	1.00	-	1.00	-	1.00
Xe134	0.32	0.33	0.33	0.32	0.35	0.36	0.35	0.33	0.2	0.34	0.6	0.39
Xe136	0.33	0.33	0.33	0.33	0.33	0.33	0.33	0.33	-	0.33	-	0.33
OFF	through cavities			direct beam				average ratio				
spacing (μm) or date	12.7	10	8	7th Feb	27th Jan	25th Jan	31st Jan	thro cavity	error %	direct	error %	natural
Xe129	0.98	1.08	1.06	0.94	0.86	0.90	0.87	1.02	3.4	0.89	1.5	0.98
Xe132	1.00	1.00	1.00	1.00	1.00	1.00	1.00	1.00	-	1.00	-	1.00
Xe134	0.31	0.33	0.32	0.31	0.33	0.32	0.35	0.32	0.4	0.33	0.8	0.39
Xe136	0.33	0.33	0.33	0.33	0.33	0.33	0.33	0.33	-	0.33	-	0.33

Fig. 4.6: The transmitted flux at various cavity spacings and in the direct beam normalised to flux at ^{132}Xe after subtracting a constant. The constant subtracted was estimated by assuming that the ratio $\frac{^{136}Xe}{^{132}Xe}$ is 0.33 within each set.

1	2	3	4	5	6	7
central mass	Flux (average over peak)	error in flux	Flux(peak-background)	ratio (column 4 rel. to 132)	error on ratio	Natural ratio rel. to 132
amu	# per sec	# per sec	# per sec			
128	20.74	2.04	8.91	0.15	0.08	0.07
129	70.78	3.76	58.95	1.02	0.03	0.98
130	24.04	2.19	12.22	0.21	0.04	0.15
131	88.07	4.20	76.24	1.32	0.02	0.79
132	69.58	3.73	57.75	1.00	-	1.00
134	31.34	2.50	19.51	0.34	0.03	0.39
136	30.42	2.47	18.59	0.32	0.04	0.33
	Average background flux	error in flux				
	11.83	0.34				

Fig. 4.7: The data of Fig. 3.5 averaged over the mass peaks. The background is estimated by averaging over regions where no atomic species exist. This background is subtracted and the isotope ratios (with respect to ^{132}Xe) are compared with natural ratios to see if there is any difference.

each mass. There is, however, one set of data in which the instrumental background is well measured and we return once again to the mass-scan data of Fig. 3.5. The flux at each species and the background are tabulated in Fig. 4.7 along with the ratio $\frac{^{m}Xe}{^{132}Xe}$ for each species. A comparison with the natural ratios shows that the passage of the atoms through the capillary arrays has not affected the natural ratios in any significant way.

The fact that the $\frac{^{129}Xe}{^{132}Xe}$ ratio has not been affected at a 3% level can be interpreted as discussed in the next section.

4.3 Difference in the Casimir-Polder interaction of ^{129}Xe and ^{132}Xe

The lighter isotope ^{129}Xe being an even-odd nucleus possesses a nuclear magnetic moment, $^{129}\mu = -0.7768$ nuclear magnetons. On the other hand the heavier isotope ^{132}Xe being an even-even nucleus has $^{132}\mu = 0$. Thus the atomic levels of ^{129}Xe would

be shifted and split due to hyperfine interactions. This difference is over and above the small difference in the isotope shift between the two. Now, we consider the question"what is the effect of these differences on the Casimir-Polder forces experienced by these two atoms?" To answer this question we begin by recalling the simplified formulation we had presented in Chapter-I for design considerations.

From Eqn. 1.10 we may define the transmission probability, P as

$$P = \frac{f_e}{f_o} = \frac{(w-\delta)^2}{w^2} \tag{4.3}$$

The formalism for calculating P through a channel of circular cross section is explicitly derived in Appendix A.

From the angle of deflection, $\triangle\theta$ the atom suffers during its traversal of the channel, given in Eqn. 1.13 we may estimate δ, the phenomenological length parameter, as

$$\begin{aligned} \delta \approx L\ \triangle\theta &= \frac{F_{CP}L^2}{k_BT} \\ &= \frac{C_pL^2}{k_BT}\ \frac{1}{z^5} \end{aligned} \tag{4.4}$$

where $C_P = 6 \times 10^{-26}$ Newtons per atom when z is in microns. Now we estimate the transmission probability of ^{132}Xe from an assumed value for ^{129}Xe by Taylor expansion:

$$\begin{aligned} {}^{132}P &\equiv P(C_p + \triangle C_p) \\ &= P(C_p) + \frac{\partial P}{\partial C_p}|_{129}\triangle C_p \\ &\equiv {}^{129}P + \frac{\partial P}{\partial C_p}|_{129}\triangle C_p \end{aligned} \tag{4.5}$$

Here $\triangle C_p$ is the difference in the Casimir-Polder coefficients for the two atoms. Straight forward manipulation yields

$$R \equiv \frac{{}^{129}P - {}^{132}P}{{}^{129}P} = \frac{1}{3}\frac{\frac{1}{W}\left(\frac{L^2C_p}{k_BT}\right)^{\frac{1}{6}}}{\left\{{}^{129}P\right\}^{\frac{1}{2}}} \cdot \frac{\triangle C_p}{C_p} \tag{4.6}$$

For large opacity $\tau = P^{-1}$ we may set

$$\frac{1}{w}\left(\frac{L^2 C_p}{k_B T}\right) \approx 1 \tag{4.7}$$

and write

$$\frac{^{129}P - ^{132}P}{^{129}P} \approx \frac{1}{3}\tau^{\frac{1}{2}}\frac{\triangle C_p}{C_p} \tag{4.8}$$

From the observation of the mass peaks in Fig. 3.5 we find that the abundance ratio reproduces the natural ratio given by IUPAC to 3% accuracy. In other words

$$R_{observed} = \frac{^{129}P - ^{132}P}{^{129}P} \leq 3 \times 10^{-2} \tag{4.9}$$

or

$$\frac{\triangle C_p}{C_p} \leq \frac{9 \times 10^{-2}}{\tau^{\frac{1}{2}}} \tag{4.10}$$

or

$$\frac{\triangle C_p}{C_p} \leq 3 \times 10^{-2} \tag{4.11}$$

for a typical opacity of the capillaries of diameter ~ 10 μm

Thus if there is any difference in the Casimir-Polder force between these isotopes it is less than 3% of the force on any one of them.

4.4 Bounds on Yukawa like forces

For distances larger than $137a_0$ and up to about 10 μm the dominant interaction between a neutral atom and a conducting surface is the Casimir-Polder interaction. An accurate measurement of this force leads to constraints on the strength and distance range of other interactions that may exist. Such interactions often are an essential consequence of the theoretical proposals to unify gravitational interaction with the Standard Model of particle physics (see [8] [2] [4], [3] and [24]). The forces arising from these interactions are small and their potentials are scaled with respect to the gravitational interaction between two point masses as shown below:

$$V(r) = -\frac{GM_1M_2}{r}\left(1+\alpha e^{-\frac{r}{\lambda}}\right) \tag{4.12}$$

Given this form for the potential constraints can be placed on the parameter space of $\alpha-\lambda$ from experiments that study long-range interactions. For distances of $\lesssim 0.1$ mm, Casimir force provides the dominant background and best limits on α for these λ have been obtained from Casimir force measurements. The Fig. 4.8 below summarizes the current status of constraints on such forces.

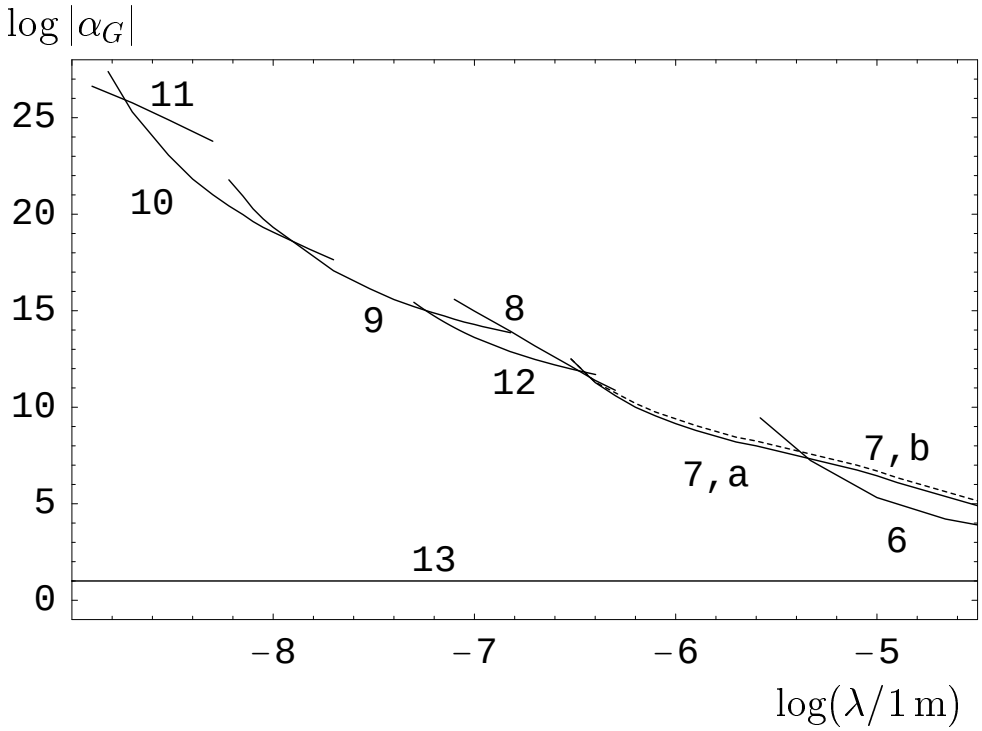

Fig. 4.8: Plot of the constraints on the Yukawa interaction parameter α for various ranges of λ reproduced from [21]. Curves 7-10, 12 follow from Casimir force measurements, Curve 11 from van der Waals force measurements. Curve 6 is from an experiment that measured deviations from Newton's law of gravity [18]. The typical prediction of extra dimensional physics is shown in Curve 13. The region, in the (α, λ) plane, above each curve is excluded and the region below each curve is allowed.

Assuming that the Yukawa force is effective only in close proximity to the walls ,

we can estimate it in the following way:

$$\begin{aligned} F_y &= 2\pi G\rho\alpha\lambda \cdot m_{Xe}\ e^{-\frac{w-z}{\lambda}} \\ &\equiv C_y\ e^{-\frac{z}{\lambda}} \end{aligned} \tag{4.13}$$

In analogy with Eqn. 4.4 we can write

$$\begin{aligned} \delta_y &= L\_\triangle\theta \\ &\approx \frac{C_y L^2}{k_B T}\ e^{-\frac{z}{\lambda}} \end{aligned} \tag{4.14}$$

Proceeding as before and assuming that ^{132}Xe does not suffer any reduction in transmission ($^{132}P = 1$) we may estimate bounds on α.

We may consider two cases:

a) Transmission through the ceramic tube. Here $\rho \approx 2.5, w \approx \lambda \approx 5 \times 10^{-4}$ cm and $L \approx 0.1$ cm the upper bound on α turns out to be

$$\alpha < 4 \times 10^{23} \quad \text{for} \quad \lambda \approx 5\mu \tag{4.15}$$

b)For transmission through the metallic slit, we take $\rho \approx 6.7, w \approx z \approx \lambda \approx 100$ μm and $L = 1.8$ cm and find

$$\alpha < 10^{16} \quad \text{for} \quad \lambda \sim 10^{-2} \text{ cm} \tag{4.16}$$

The bounds are decidedly much poorer than those obtained from torsion balance studies. We derive them here merely because they pertain to atoms with finite nuclear spin (unpolarized) and magnetic moment.

5. PROSPECTS FOR FUTURE EXPERIMENTS

Abstract

In this chapter we present a brief review of the experimental efforts by various groups around the world towards investigating atom surface interactions with specific reference to testing the QED predictions. These experiments are at times not in agreement with each other. Indeed in some of them, inclusion of the Casimir-Polder potential results in a poorer fit to the data. Therefore the understanding of the atom-surface interactions at one to ten micron distance range still poses several challenges. Towards the end of the chapter we describe an experimental scheme which could circumvent some of the problems faced in these experiments.

5.1 Introduction

The study of the atom surface interactions has been explored by many researches with systems widely different from each other. While there is broad qualitative agreement between their results there are differences in detail. As yet these differences are not well understood and often it is suspected that stray electric charges or patch potentials in the deposited metal layers gives rise to these deviations. The experiment with the highest precision, that of Sukenik et al. [31], finds the theory in agreement with their observations to 10% accuracy. The deviation they observe at 0.67 μm is possibly due to the finite conductivity of the gold coatings. With metastable atoms slowed to velocities $\approx$ 1 cm.s^{-1} Aspect et al. [6] and Shimizu [28] have observed the van der Waals interaction at distances up to $\approx$ 100 nm. While the experiments have not yet reached the sensitivity to probe the interaction at larger distances explicitly, they do

have to include a Casimir-Polder term to obtain a good fit to the data. In the most recent experiment by Yu-ju et al.[14] they use a BEC and ultra-cold thermal atoms to probe the potential. While their findings are in good agreement with theory for a dielectric surface they see deviations for metallic surfaces. These experiments are reviewed in the following sections.

The strength of the Casimir-Polder force is significantly reduced when the atom is placed between two surfaces since in this case it will experience only the difference of two opposing forces. A scheme which would retain the strength of the force from a single surface, while not compromising on the advantages of maintaining a good control over the allowed range of impact parameters, is described in the last section.

5.2 A brief review of several recent experiments

The work by Hinds [31] and his co-workers at the Yale university has been discussed in detail in Chapter 1. They studied the deflection of a beam of Sodium atoms caused by this force as they traversed a micron wide channel formed by two conducting plates. In their experiment ground state Sodium atoms emerged from a vertical slit into a high vacuum chamber and formed the atom beam. The atoms then passed through a long narrow vertical channel between two gold coated optical flats which formed a small angle wedge. The atoms, which successfully traversed through the channel, were ionized and counted. Ionisation involved two steps - first the atoms were excited to the 14S Rydberg state by two lasers (589 nm and 420 nm) and then field ionized. These ions were counted by a channeltron detector. The laser beams are both focussed so that detection occurs over a small height($\approx$ 200 μm), corresponding to a well defined channel width. They observed that the transmission of the atomic beam through the channel dropped below the geometric value as the plate separation was reduced from 2 μm towards smaller values. They could interpret this reduction as due to the loss of some of the atoms in the beam which got deflected by the Casimir-Polder (CP) force, hit the walls of the channel and were lost from the beam.

In a later experiment Storry et.al. [30] of the York University, Toronto, carried out a high-precision spectroscopic measurement of the n=10 $^{+}G_4$ - $^{+}F_3$ transition in a helium atom beam. This transition frequency has been theoretically computed to a high precision by Drake [9] and they predict a frequency of 2017.3242(4) MHz. The interaction potential used in this calculation includes the retardation (Casimir) corrections. However the measured frequency is 2017.3254(4) MHz, which is 1.2kHz above the theoretically predicted value. The discrepancy is 2.4 times the combined theoretical and experimental uncertainties. Thus this measurement finds no signature of the Casimir interaction. A second possible interpretation of this data is that the Casimir-Polder interaction is indeed present and that there are also other significant interactions indicating new long range physics.

In a recent experiment Coget et.al. [6] [25] observed the diffraction of atoms incident on an evanescent wave grating at a grazing angle. However ordinary scalar diffraction, which does not depend on the internal states of the atom or the polarization state of the grating lines, is strongly suppressed because the atomic phase calculated along a classical trajectory is averaged out over many grating periods. Thus the large diffraction angles can only be understood as resulting from atomic changes of state. The energy transfer corresponding to the momentum change perpendicular to the plane of the grating comes from the difference in the light shifts of the initial and the final states. The magnitude of the light shift and hence the diffraction probability is a sensitive function of the van der Waals' interaction potential. The observations show a signature of the short range van der Waals' interaction and the experiment can be extended to see the CP interaction as well.

With atoms that are incident on a solid surface at extremely low incident velocity (1 mm to 3 cm per sec) Shimizu [28] observed that they undergo a specular reflection. This reflection arises due to the fact that when atomic motion is sufficiently slow the associated de Broglie wavelength becomes large and indeed approaches macroscopic length scales. If the atom encounters a sharp potential change such that the length of the local wave-vector, $\overrightarrow{k}$ changes by large amounts ($> k^2$) over a small distance (k)

then it is reflected back with a certain probability. Shimizu performed an experiment wherein they dropped cold metastable Ne atoms from a height on to a glass or a silicon surface at grazing incidence. The atoms were detected using a multi-channel plate (MCP) place at the bottom. To identify the various components of the incident cloud (scattered, specularly reflected etc) they introduced a mask in between the source of cold atoms (a magneto optic trap) and the solid surface. They could then interpret the pattern of atoms that arrived at the MCP to indicate specular reflection of atoms with reflection co-efficients up to 30% for the lowest of incident velocities (about 1mm per sec). They varied the mean incident velocity of the cloud by changing the angle of incidence on the surface. Thus they obtained a reflectivity versus incident velocity dependance which could then be analysed to obtain the nature of the atom-surface potential. Though the accuracy of the experiment was not sufficient to allow a detailed quantitative analysis, their results showed that the reflection occurs from an attractive potential which is a combination of the van der Waals and Casimir-Polder potentials.

Yu-ju Lin and co-workers [14] aim to achieve full quantum control over the motion of ultra-cold atoms by using controlled quantum reflection at miniaturised field sources. They use thermal clouds and Bose-Einstein condensates of Rb atoms trapped in a Ioffe-Pritchard trap, which is created by passing currents through microfabicated conductors on a silicon chip. They however encounter instabilities in the trapping potential when the trap approaches the structures on the chip surface. They investigated these instabilities, both when the trap approaches a dielectric (Si_3N_4) surface and when it approaches a conductor (copper strip). They record the mean life time of the trapped atoms as a function of distance of the trap from the surface. They then obtain theoretical fits to the measured lifetimes for a combined trap and Casimir-Polder potentials. Though the experimental errors are large their results are in agreement with the theoretical expectation for the Si_3N_4 surface. However there are systematic deviations from the theory in the case of the metallic surface. The reason for the observed discrepancy is not well understood. Patch potentials from Rb atoms adsorbed on the surface of the metal could be a possible cause of this discrepancy.

5.3 Future directions

The analysis of the data thus far acquired shows that several problems need to be addressed in the experiment before we can succeed in measuring the atom-wall potential. First the fluctuations in gain which arise when we change a mass-setting in the RGA have to be addressed. These fluctuations are not seen to occur when we adjust the mass-setting in small steps. Therefore the data has to be acquired not at discreet masses but in a scan as in the Fig. 3.5. This would have the added advantage that the instrumental noise is also sampled in every run and thus will enable us to subtract it with confidence. The measurement of flux at various cavity widths has to be done within a short time of each other so that the variation in background between measurement is not great. The background also has to be measured in between every two scans so that we will be able take into account the slow variations in the background density and effects due to thermal fluctuations. It would also be desirable to increase the length to diameter ratio of the capillaries as the beam intensity to total throughput is directly proportional to this ratio under optimal operating conditions.

In the beginning of our research activities we adopted the scheme followed by the Yale group for the measurement of the Casimir-Polder forces. Their configuration overcame the intrinsic difficulties in specifying the impact parameters in the set-up used by Raskin and Kusch. In the future experiments we may consider using the Yale scheme, with a few modifications as indicated in Fig. 5.1 :

The channel consists of one conducting surface and a sequence of knife-edges whose edges form a plane limiting the range of impact parameters. This scheme may result in the following advantages:

a) The Casimir-Polder force decreases from the surface as $\sim z^{-5}$, so that in the parallel plate geometry shown in Fig. 1.3 the force experienced by an atom at a distance z from the median plane may be approximated as,

$$F_{CP}^{Y} = A\left[\frac{1}{(w-z)^5} - \frac{1}{(w+z)^5}\right] \tag{5.1}$$

This has a value $F_{CP}^{Y}(z=0)=0$ on the median plane; and further more $\frac{\partial F_{CP}^{Y}}{\partial z}$=0 on the median plane. Thus there is always a substantial region near the center where

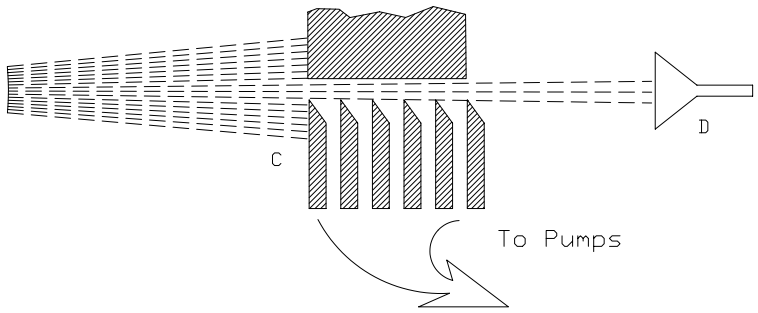

Fig. 5.1: Scheme for increasing the effect of the Casimir-Polder force and reducing the background due to the 'bouncers'.

the force is zero and transmission always occurs through this, reducing the Casimir-Polder opacity of the channel. In contrast the new scheme sketched in Fig. 5.1, generates a force field

$$F_{CP}^{Y} = A\left[\frac{1}{(w-z)^5}\right] \tag{5.2}$$

This is truly a long-range field without any cut-off. The ratio of the two fields is given by

$$\eta = \frac{F_{CP}^{N}}{F_{CP}^{Y}} = \frac{(w+z)^5}{(w+z)^5 - (w-z)^5} \tag{5.3}$$

b) The second advantage of this set-up is that few of the atoms that hit the surface do make their way to the end of the channel adding to the observed flux. These are called "bouncers" by the Yale group. The bouncer-flux increases with cavity width and limits the range up to which the Casimir-Polder interaction might be studied. In the scheme sketched here the knife-edges act as "skimmers" preventing the bouncers from reaching the detector. These are easily pumped away through a side port in the channel.

c) Futher more this scheme allows the search for spin dependant interactions of the kind $\overrightarrow{r} \cdot \overrightarrow{d}$ suggested by Moody and Wilczek [11].

APPENDIX

A. CALCULATION OF TRANSMISSION THOUGH A TUBE

Objective: Calculate the probability that a particle starting at $\overrightarrow{r_i}$ with velocity $\overrightarrow{v_i}$ will traverse the tube (Radius, R, and length L) without, hitting its inner walls.

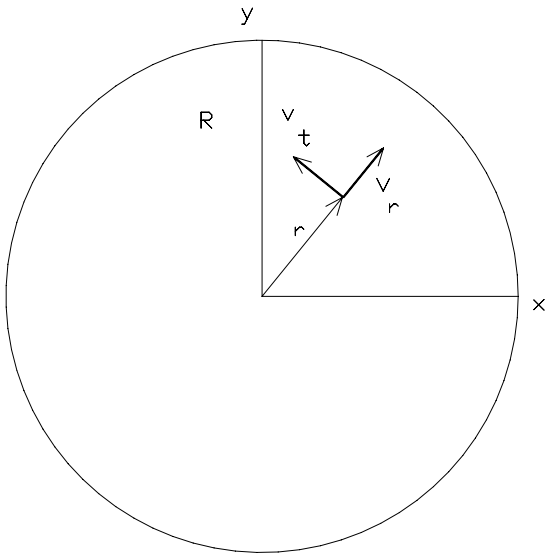

Fig. A.1: The co-ordinate system for the calculation of transmission though a tube

Theoretical Considerations:

Consider a particle inside the tube at a position (r, θ) with velocity (v_r, v_t) (see Fig. A.1). We first calculate the time taken by the particle to hit the walls. From this we compute the probability that it will exit the tube before the elapse of this time. We then integrate over the space of initial conditions, with the appropriate probability density functions as the weights to obtain the flux of atoms through of the tube.

The prescription for calculating the time of flight is as follows: The calculation is

simplified by noting that the gradient in potential U due to the walls is always in the r direction. Thus it has the simplicity of a central force problem, with the angular momentum J and energy E as conserved quantities.

The two conserved quantities are:

$$E = \frac{1}{2}m\left(v_t^2 + v_r^2\right) + U(r) \tag{A.1}$$

$$J = m\ r\ v_t \tag{A.2}$$

Using Eqn. A.2 the energy equation is written as,

$$E = \frac{J^2}{2mr^2} + \frac{1}{2}mv_r^2 + U(r). \tag{A.3}$$

Setting $v_r \equiv \dot{r}$, we get

$$\dot{r} = \frac{dr}{dt} = \left\{\frac{2}{m}\left[E - U(r) - \frac{J^2}{2mr^2}\right]\right\}^{1/2} \tag{A.4}$$

The radial co-ordinate of the particle is calculated iteratively from the initial conditions defined by: $r(0), E, J$,

$$r(new) = r(old) + \left(\frac{dr}{dt}\right)\Big|_{n-1} \triangle t + \frac{1}{2}\frac{d^2r}{dt^2}\Big|_{n-1} \triangle t^2 \tag{A.5}$$

The time of flight (t) of the particle is given by $n \cdot \triangle t$ where n is the number of iterations that were necessary for the particle to reach the wall (at $r = R$) and $\triangle t$ is the time step that with which the iteration propagates the particle.

In the absence of an interaction ($U(r) = 0$) the time of flight can be analytically computed as follows: Consider a particle at a distance x from the center as shown in Fig. A.2. If the were to particle travel a distance S before it hits the wall then the following geometric relation holds:

$$(2x_0 \cos\theta + S)S = (a + x_0)(a - x_0) \tag{A.6}$$

The distance S will therefore be

$$S = -x_0.c \pm \sqrt{a^2 - x_0^2(1 - c^2)} \tag{A.7}$$

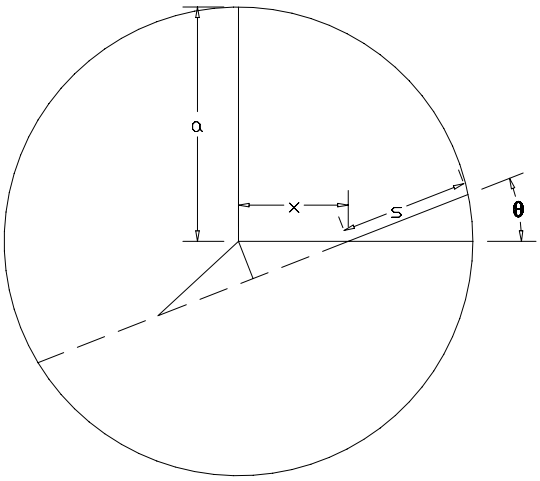

Fig. A.2: The geometry for calculating the time of flight for free particle inside the tube. The tube is seen end on.

where $c = cos(\theta)$ given by

$$c = \frac{v_r}{\sqrt{v_t^2 + v_r^2}} \tag{A.8}$$

with θ being the angle between the position and velocity vectors.

Then the time of flight is

$$t \;=\; \frac{|\,S\,|}{\sqrt{v_t^2 + v_r^2}} \tag{A.9}$$

We now turn to the evaluation of the probability of transmission. Let $p(r,\ \phi,\ v_r,\ v_t)$ be the probability of a particle passing though the tube starting at an initial position (r, θ) with an initial velocity (v_r, v_t). To obtain the flux (no. of atoms per sec) passing through the tube we need to integrate probability over the space of all possible initial positions and velocities weighted by their respective probability density functions.

It is convenient to cast the integration in cartesian co-ordinates while noting the following essential constraint:

$$\begin{aligned} &\int p(r,\ \phi,\ v_r,\ v_t)\ p(r)\ r dr\ p(\phi)\ d\phi\ p(v_r)\ dv_r\ p(v_\phi)\ dv_\phi \;\; = \\ &\int p(x,\ y,\ v_x,\ v_y)\ p(x)\ p(y)\ p(v_x)\ p(v_y)\ dx\ dy\ dv_x\ dv_y \end{aligned} \tag{A.10}$$

where $p(x,\ y,\ v_x,\ v_y)$ is the probability of a particle passing though the tube starting with $x_0 = x,\ y_0 = y,\ v_{x0} = v_x,\ v_{y0} = v_y,\ v_{z0} = v_z$ and is given by,

$$p(x,\ y,\ v_x,\ v_y) = \left(\frac{m}{2\ \pi\ k\ T}\right)^{1/2} \int_{\left[\frac{t_{min}(x,y,v_x,v_y)}{L}\right]^{-1}}^{\infty} v_z\ e^{-\frac{mv_z^2}{2kT}}\ dv_z \tag{A.11}$$

Note that $p(r,\ 0,\ v_r,\ v_t) = p(x,\ 0,\ v_x,\ v_y)$ for $r = x; \phi = 0;\ y = 0;\ v_r = v_x;\ v_t = v_y$. Further more $p(\phi) = 1$. Thus, we get the total flux through the tube as,

$$2 \int p(x = r,\ 0,\ v_x = v_r,\ v_y = v_t) \left(\frac{m}{2\ \pi\ k\ T}\right) dv_x\ dv_y\ e^{-\frac{(v_x^2+v_y^2)\ m}{2kT}}\ 2\pi x\ dx \tag{A.12}$$

The range of integration in Eqn. A.12 above is over the domain $0 < x < r_t,\ -v_{xmax} < v_x < v_{xmax},\ 0 < v_y < v_{ymax}$.

BIBLIOGRAPHY

[1] Heckel B. R. Stubbs C. W. Rogers W. F. Adelberger, E. G. Searches for New Macroscopic Forces. *Ann. Rev. of Nuclear and Particle Science*, 41:269, December 1991.

[2] I. Antoniadis, N. Arkani-Hamed, S. Dimopoulos, and G. Dvali. New Dimension at a Millimeter to a Fermi and Superstrings at a TeV. *Phys. Lett. B*, 436:257, 1998.

[3] N. Arkani-Hamed. Large Extra Dimensions: A new Arena for Particle Physics. *Physics Today*, page 35, Feb. 2002.

[4] N. Arkani-Hamed, S. Dimopoulos, and G. Dvali. The Hierarchy Problem and New Dimension at a Millimeter. *Phys. Lett. B*, 429:268, 1998.

[5] Casimir, H. B. G.,Polder, D. The influence of retardation on the London-van der Waals forces. *Physical Review*, 73:360–372, 1948.

[6] L Cognet, V. Savalli, G. Zs. K. Horvath, D. Holleville, R. Marani, N. Westbrook, C. I. Westbrook, and A. Aspect. Atomic Interference in Grazing Incidene Diffraction fron an Evanescent Wave Mirror. *Phys. Rev. Lett*, 81(23), 1998.

[7] Raskin D. and P. Kusch. Interaction between a Neutral Atomic or Molecular Beam and a Conducting Surface. *Phys. Rev.*, 179:712, March 1969.

[8] S. Dimopoulos and G. F. Giudice. Macroscopic Forces from Supersymmetry. *Phys. Lett. B*, 379:105, 1996.

[9] G. W. F. Drake. New variational techniques for the 1snd states of helium. *Physical Review Letters*, 59:1549–1552, October 1987.

[10] Drexhage, K, H. . *Progress in Optics*, 12:163, 1974.

[11] Moody J. E. and Wilczek F. *Phy. Rev. D*, 30:130, 1984.

[12] E. Fishbach and Talmadge C. *The Search for Non-Newtonian Gravity*. Springer, Newyork, 1999.

[13] E. A. Hinds and Schnell M. Lai K. S. *Atoms in micron-sized metallic and dielectric wave guides*.

[14] Yu ju et al. Impact of the casimir-polder potential and johnson noise on bose-einstien condensate stability near surfaces. *Phy. Rev. Lett*, 92(5):050404–1, 2004.

[15] Krishnakumar, E. and S. K. Srivastava. Ionisation Cross sections of rare-gas atoms by electron impact. *J. Phys. B*, 21:1055, March 1988.

[16] Levin, F. S.,Micha, D. A. *Long-Range Casimir Forces*. Plenum Press, 1993.

[17] J. C. Long et al. New experimental limits on macroscopic forces below 100 microns . *ArXiv High Energy Physics - Phenomenology e-prints*, September 2002.

[18] J. C. Long et al. Upper Limit on Submillimeter-range Forces from Extra Space-time dimensions. *Nature*, 421:924, 2003.

[19] W. P Milonni. *The Quantum Vacuum: An Introduction to Quantum Electrodynamics*. Academic Press, Newyork, 1994.

[20] Moore, J. H., Davis, C. C, Coplan, M. A. *Building Scientific Apparatus*. Westview Press, 3 edition, 2003.

[21] V. M. Mostepanenko. Constraints on Non-Newtonian Gravity from Recent Casimir Force Measurements. *ArXiv General Relativity and Quantum Cosmology e-prints*, November 2003.

[22] V. M. Mostepanenko and Trunov N. N. *The Casimir Effect and its applications*. Oxford University Press, Newyork, 1997.

[23] E. M. Purcell, H. C. Torrey, and R. V. Pound. Resonance Absorption by Nuclear Magnetic Moments in a Solid. *Physical Review*, 69:37–38, January 1946.

[24] L. Randall. Extra Dimensions and Warped Geometries. *Science*, 296:1422, 2002.

[25] V. Savalli, D. Stevens, J. Esteve, P. D. Featinby, V. Josse, N. Westbrook, C. I. Westbrook, and A. Aspect. Specular Reflection of Matter Waves from a Rough Mirror. *Phys. Rev. Lett*, 88(25), 2002.

[26] A. Shih. van der Waals forces between a Cs atom or a CsCl molecule and metal or dielectric surfaces. *Physical Review A*, 9:1507, 1974.

[27] Shih, A., Raskin, D., Kusch, P. Investigation of the interaction potential between a neutral molecule and a conducting surface. *Physical Review A*, 9:652, 1974.

[28] F. Shimizu. Specular reflection of very slow metastable neon atoms from a solid surface. *Phy. Rev. Lett.*, 86(6):987, 2001.

[29] Steckelmacher, W., Strong, R. and Lucas, M. W. A simple atomic or molecular beam as target for ion-atom collision studies. *Phys. Lett. B*, 11:1553, 1978.

[30] C. H. Storry and E. A. Hessels. Separated-oscillatory-field measuremnt of the n=10 F3-G4 interval in helium: A 200-part-per-billion measurement. *Phys. Rev. A*, 55:967, 1997.

[31] C. I. Sukenik, M. G. Boshier, D. Cho, V. Sandoghdar, and E. A. Hinds. Measurement of the Casimir-Polder Force. *Phys. Rev. Lett*, 70(5):560, 1993.